



A Backdrivable Kinematically Redundant (6+3)-Degree-of-Freedom Hybrid Parallel Robot for Intuitive Sensorless Physical Human–Robot Interaction

Kefei Wen , Tan Sy Nguyen, David Harton, Thierry Laliberté , and Clément Gosselin , *Fellow, IEEE*

Abstract—A novel backdrivable 3- $\underline{R}(\underline{RR}\text{-}\underline{RRR})\underline{SR}$ kinematically redundant (6+3)-degree-of-freedom (DOF) spatial hybrid parallel robot with revolute actuators is proposed for low-impedance physical human–robot interaction. The kinematic model is developed based on the constraint conditions of the robot. It is shown that the type II (parallel) singularities can be completely avoided, thereby yielding a very large translational and orientational workspace. A workspace analysis is presented in order to demonstrate the capabilities of the robot. Mechanisms are then introduced to use the redundant DOF of the robot to operate a gripper with the robot actuators, which are mounted on or close to the base, thus reducing the inertia of the moving parts. The architecture of the robot makes it possible to use direct drive motors, thereby making the robot easily backdrivable and allowing the use of a very simple and effective controller. A prototype of the robot is then designed and built and the large workspace of the robot as well as the effortless physical human–robot interaction are demonstrated. The controller of the robot is then described, including a position control mode and a control mode for physical interaction, which does not require the use of a force/torque sensor or joint torque sensors. Because of its backdrivability and low moving inertia, the robot is particularly well-suited for physical human–robot interaction, as demonstrated in the accompanying videos.

Index Terms—Hybrid robot, kinematic redundancy, orientational workspace, parallel robot, physical human–robot interaction, remotely operated gripper, singularities.

Manuscript received July 7, 2020; revised October 15, 2020; accepted November 6, 2020. Date of publication December 24, 2020; date of current version August 5, 2021. This work was supported in part by the Natural Sciences and Engineering Research Council of Canada (NSERC), in part by the Canada Research Chair program, and in part by the *Fonds Québécois de la Recherche sur la Nature et les Technologies* (FRQNT). This article has supplementary downloadable material available at <https://doi.org/10.1109/TFUZZ.2019.2933787>, provided by the authors. This paper was recommended for publication by Associate Editor Q. Li and Editor E. Yoshida upon evaluation of the reviewers' comments. (Corresponding author: Clément Gosselin.)

The authors are with the Department of Mechanical Engineering, Université Laval, Québec, QC G1V 0A6, Canada (e-mail: kefei.wen.1@ulaval.ca; tan-sy.nguyen.1@ulaval.ca; david.harton.1@ulaval.ca; thierry@gmc.ulaval.ca; gosselin@gmc.ulaval.ca).

This article has supplementary material provided by the authors and color versions of one or more figures available at <https://doi.org/10.1109/TRO.2020.3043723>.

Digital Object Identifier 10.1109/TRO.2020.3043723

I. INTRODUCTION

PHYSICAL human–robot interaction (pHRI) is a desirable paradigm in many applications. In manufacturing, for example, the ability for a human being to guide a robot by directly manipulating its end-effector or its limbs opens the avenue to the concept of robot coworker, which can, in turn, provide a means of combining the strength and repeatability of robots with the adaptability of human workers [1]. In order to provide an intuitive physical interaction between a human being and a robot, the robot must smoothly react to the forces applied on it by the person. This compliance can be implemented passively or actively. As recalled in [2], an active pHRI system is one in which the reaction of the robot to external forces is produced using sensors (force/torque sensors or joint torque sensors) and feedback control. The control of most pHRI robots is based on this approach, including those using series elastic actuators [3] and industrial cobots [4]. Force and torque sensors are necessary in such robots since they are not mechanically backdrivable, mainly due to the use of harmonic drives to reduce the requirements on actuator torques. On the other hand, in backdrivable robotic systems, the forces applied on the robot links can be directly sensed by the actuators by measuring motor currents or even simply displacements. As pointed out in [2], [5], and [6], this approach allows the actuators to also act as torque sensors, thereby greatly easing the dynamic stability of the control of the interaction. However, backdrivable robotic joints are difficult to implement in serial robots because of the size and mass of the actuators that are required to produce sufficiently large torques. An example of a quasi-backdrivable serial robot is presented in [2], although with a limited payload and low dynamics.

A possible approach to circumvent the above issues is to use a parallel or hybrid robot, in which the actuators can be mounted on or close to the base. Using this arrangement, direct-drive or quasi-direct-drive actuators become possible, without compromising the robot's moving inertia, payload, or dynamic capabilities.

Several parallel manipulators have been proposed in the literature for the force-controlled interaction with a physical environment (see, for instance, [7]–[9]) or with humans [10]. However, their control is based on force or torque sensors due to the non-backdrivability of the robots. In [10], the term “sensorless”

is used to indicate that there is no force/torque sensor at the end-effector. However, the controller relies on the torque sensors at the actuators, which are not backdrivable. Moreover, the six-degrees-of-freedom (DOF) parallel manipulators proposed in the literature have limited rotational capabilities, which is a significant deterrent for pHRI applications. Indeed, in such applications, it is desired that the human operator be capable of guiding the robot within a large orientational workspace in order to provide intuitiveness (translational workspace can always be increased by scaling up the robot).

In this article, the two main limitations mentioned above are addressed. First, kinematic redundancy is used to extend the orientational workspace of a hybrid parallel robot to make it suitable for pHRI. Second, direct-drive actuators located on or close to the base are used to produce mechanical backdrivability and very intuitive pHRI. Moreover, since the moving inertia of the robot is very low, a special case of impedance control can be used in which the impedance rendered to the user is the real mechanical impedance of the robot, yielding a very simple and robust controller.

A. Kinematic Redundancy in Parallel Robots

Novel kinematically redundant parallel robots have been recently proposed (see, for instance, the following planar [11], SCARA [12], and spatial 6-DOF [13] robots), where the authors focused on the enlargement of the orientational workspace, which is an important benefit of using kinematic redundancy. In [14], the redundancy resolution of the robot proposed in [13] is presented. Algorithms are developed in order to resolve the redundancy while avoiding singularities. Although the effectiveness of the numerical algorithms is successfully demonstrated, the singularity avoidance cannot be expressed in closed form.

B. Contents and Organization of the Article

In this article, we propose a three-legged revolute joint actuated (6+3)-DOF kinematically redundant hybrid parallel robot that can be regarded as the redundant counterpart of the 3-[R(RR-RRR)S] platform studied in [15] and [16]. Using only three legs can help to avoid leg interferences and interferences with the environment, which is an important feature in the context of pHRI. The robot is driven by nine motors: three per leg. Each of the legs is then connected to the moving platform via a redundant link. The axes of the revolute joints connecting the redundant links to the platform are parallel. Using this arrangement, it is shown that type II singularities can be completely avoided. Moreover, the singularity analysis—which is readily conducted using Grassmann line geometry (GLG)—yields very simple conditions. Consequently, a closed-form solution of the inverse kinematics, including the avoidance of singularities, can be obtained without having to resort to numerical algorithms, which greatly simplifies the trajectory planning of the robot.

This article is based on the conference paper [17], in which the concept of the robot was first introduced. In this article, the architecture and the kinematics of the robot are first recalled. Then, the workspace of the robot and the singularity analysis are further investigated. A prototype of the robot is presented for

the first time. The control of the robot is addressed and a scheme is proposed for the pHRI control of the redundant parallel robot in which the user input does not completely constrain the configuration of the robot. Then, experimental results and videos are provided in order to demonstrate the low-impedance and high-bandwidth properties of the prototype.

This article is structured as follows. A description of the architecture of the proposed robot is given in Section II, followed by the development of the kinematic model in Section III. Then, GLG is applied in Section IV to analyze the type II singular conditions of the robot. It is shown that type II singularities are easily avoidable without requiring special trajectory planning. Sections V and VI, respectively, address the inverse kinematics and the forward kinematics of the robot. Then, in Section VII, it is shown that the proposed robot has a very large singularity-exempt rotational and translational range of motion. In Section VIII, a mechanism using the joints at the platform is proposed to exploit the redundancy of the robot in order to operate a gripper, while avoiding singularities. Using this mechanism, the gripper is operated directly from the motors located at or near the base of the robot. The prototype of the robot designed and built in this work is then described in Section IX. In Section X, the controller of the robot is described, which includes a position control mode and an interactive control mode. Section XI presents experimental results. Although no force/torque sensor is used in the controller of the robot, such a sensor is mounted on the end-effector of the robot in some of the experiments to collect data in order to demonstrate the capability of the robot to provide a low-impedance high-bandwidth interaction with a human user. In Section XII, the videos accompanying this article are described. The videos demonstrate the large workspace of the robot, its dynamic capabilities, and the intuitiveness of the pHRI that it provides. Finally, Section XIII concludes this article.

II. ROBOT ARCHITECTURE

The architecture of the proposed robot consists of a moving platform connected to the base by three identical kinematically redundant R(RR-RRR)SR legs, as shown in Fig. 1. Here, R stands for an actuated revolute joint, R stands for a passive revolute joint, and S stands for a passive spherical joint. In each of the legs, a first actuated revolute joint is mounted at the base. Then, two actuated revolute joints with collinear axes are mounted on the first moving link and are used to actuate two bars of a planar five-bar linkage (see Figs. 1 and 2). The combination of these three actuated joints is used to position the spherical joint of the i th leg (point S_i) in space, as illustrated in Fig. 2. As shown in Figs. 1 and 2, the spherical joint at point S_i is then connected to a link that is, in turn, connected to the moving platform using a revolute joint. A description of the geometric parameters used to model the kinematics of the robot is given in Fig. 2.

In the model, l_{ij} , ($i = 1, 2, 3; j = 2, \dots, 7$) denotes the length of the j th link of the i th leg and s_{ij} , ($i = 1, 2, 3; j = 2, \dots, 7$) is a vector defined along link ij of the i th leg—of length l_{ij} —as illustrated in Fig. 2. Also, vector s_{i1} is pointing from the origin of the base frame to the point of intersection of the axes of the

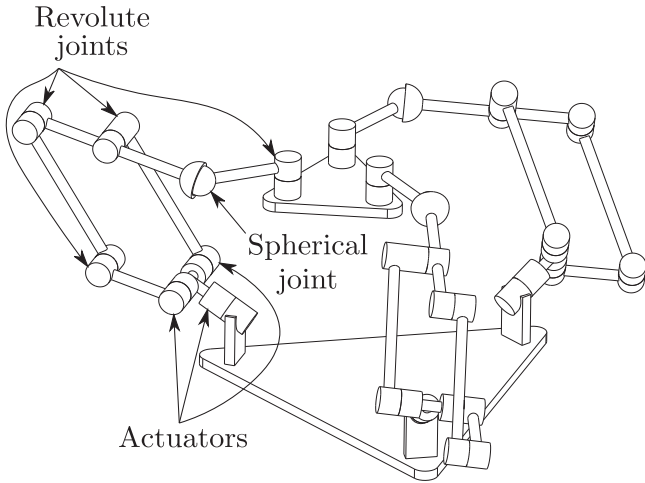


Fig. 1. Architecture of the proposed hybrid parallel robot.

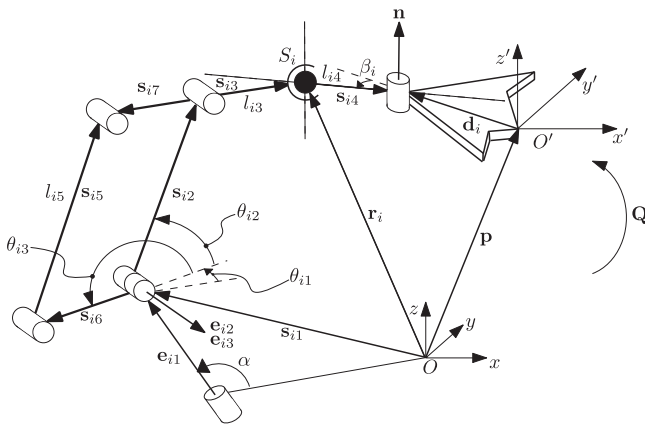


Fig. 2. Geometric description of one leg.

three actuated joints of the i th leg. The axes of all the joints in the planar five-bar linkage are parallel to each other and perpendicular to the axis of the first joint of the leg. Also, the axis of the revolute joint attached to the platform is perpendicular to the plane of the platform, formed by the three attachment points of the legs. The actuated joints $i2$ and $i3$ at the base of the planar five-bar linkage are associated with unit vectors \mathbf{e}_{i2} and \mathbf{e}_{i3} . In order to keep away from type I (serial) singularities, which occur when the center of joint S_i is located on the axis of the first actuated joint of the leg—associated with unit vector \mathbf{e}_{i1} —links $i1$ (located between the first and the following two coaxial revolute joints of the i th leg) are designed to make an obtuse angle with respect to the base which is the angle described as α in Fig. 2. In the final design, angle α is selected to be equal to π . This is the optimal selection to prevent type I singularities if the base of the robot is considered as the lower limit of the workspace. Indeed, in this case, the singular configurations are located outside of the workspace of the robot. In order to reduce the effect of the inertia of motors $i2$ and $i3$, they are placed as close as possible to the axis of the first actuator, as illustrated in Fig. 2. These motors drive, respectively, links $i6$ and $i2$ of

the planar five-bar linkage. As opposed to many other spatial parallel mechanisms in which the S joints are directly attached to the platform (for instance, in [15]), in the present robot, they are located between links $i3$ and $i4$. Such an arrangement, along with the particular direction of the axis of the R joint attached to the platform—which is orthogonal to the plane of the platform—yields advantages for the singularity and inverse kinematic analysis, as shown in the upcoming sections of the article. It should also be pointed out that because of the extra link between the S joints and the platform, the mechanism has nine DOFs and nine actuators (three in each leg) which means that the redundancy is purely kinematic. Therefore, there is no actuation redundancy, and no antagonistic forces are generated by the actuators.

III. KINEMATIC MODELLING

A base frame and a moving frame are respectively attached to the centroids of the base and moving platform, which are noted as $Oxyz$ and $O'x'y'z'$ (see Fig. 2). Vector \mathbf{p} represents the position of O' with respect to O and matrix \mathbf{Q} represents the orientation of the moving platform with respect to the base. Vector \mathbf{r}_i denotes the position of S_i . Vector \mathbf{n} is the unit vector along the axis of the revolute joint attached to the platform and \mathbf{d}_i is the position vector of the center of the revolute joint that is attached to the platform, which is expressed in the moving frame. Except for \mathbf{d}_i , all vectors are expressed in the base frame. The constraint equations of the robot, which are used to derive the kinematics, can be written as follows. First, the constraint on the length of the fourth link is written as

$$(\mathbf{p} + \mathbf{Q}\mathbf{d}_i - \mathbf{r}_i)^T (\mathbf{p} + \mathbf{Q}\mathbf{d}_i - \mathbf{r}_i) = l_{i4}^2, \quad i = 1, 2, 3. \quad (1)$$

Also, the fourth link must be orthogonal to the axis of the R joint attached to the platform, which yields

$$\mathbf{n}^T (\mathbf{p} + \mathbf{Q}\mathbf{d}_i - \mathbf{r}_i) = 0. \quad (2)$$

Equations (1) and (2) are the geometric constraints of the robot. Equation (1) is first considered. The time derivative of (1) yields

$$\mathbf{s}_{i4}^T \dot{\mathbf{p}} + \mathbf{s}_{i4}^T \dot{\mathbf{Q}}\mathbf{d}_i = \mathbf{s}_{i4}^T \dot{\mathbf{r}}_i \quad (3)$$

where

$$\mathbf{s}_{i4} = \mathbf{p} + \mathbf{Q}\mathbf{d}_i - \mathbf{r}_i. \quad (4)$$

The second term on the left-hand side of (3) can be written as

$$\mathbf{s}_{i4}^T \dot{\mathbf{Q}}\mathbf{d}_i = \mathbf{s}_{i4}^T \Omega \mathbf{Q}\mathbf{d}_i = \mathbf{s}_{i4}^T [\boldsymbol{\omega} \times (\mathbf{Q}\mathbf{d}_i)] = [(\mathbf{Q}\mathbf{d}_i) \times \mathbf{s}_{i4}]^T \boldsymbol{\omega} \quad (5)$$

where $\boldsymbol{\omega}$ is the angular velocity vector of the platform and Ω is the angular velocity tensor, i.e.,

$$\dot{\mathbf{Q}} = \Omega \mathbf{Q}. \quad (6)$$

Also the right-hand side of (3) can be written as

$$\mathbf{s}_{i4}^T \dot{\mathbf{r}}_i = \mathbf{s}_{i4}^T (\mathbf{M}_i \dot{\boldsymbol{\theta}}_i) = \mathbf{k}_i^T \dot{\boldsymbol{\theta}}_i \quad (7)$$

where $\dot{\boldsymbol{\theta}}_i = [\dot{\theta}_{i1} \ \dot{\theta}_{i2} \ \dot{\theta}_{i3}]^T$ is the vector of actuated joint velocities of the i th leg, while

$$\mathbf{k}_i^T = \mathbf{s}_{i4}^T \mathbf{M}_i, \quad i = 1, 2, 3 \quad (8)$$

is a 1×3 line vector, and \mathbf{M}_i is the Jacobian matrix of the i th leg when considered as a 3-DOF robot that is used to position point S_i . This matrix is readily obtained by considering the kinematics of the leg, as shown in Fig. 2. The detailed derivation is given in Appendix A. One obtains

$$\mathbf{J}_i \dot{\mathbf{r}}_i = \mathbf{W}_i \dot{\boldsymbol{\theta}}_i, \quad i = 1, 2, 3 \quad (9)$$

where

$$\mathbf{J}_i = \begin{bmatrix} \mathbf{e}_{i2}^T \\ \mathbf{s}_{i3}^T \\ -\frac{l_{i7}}{l_{i3}} \mathbf{s}_{i5}^T \end{bmatrix} \quad (10)$$

and

$$\mathbf{W}_i = \begin{bmatrix} w_{i11} & 0 & 0 \\ 0 & \mathbf{s}_{i3}^T (\mathbf{e}_{i2} \times \mathbf{s}_{i2}) & 0 \\ 0 & w_{i32} & \mathbf{s}_{i5}^T (\mathbf{e}_{i3} \times \mathbf{s}_{i6}) \end{bmatrix} \quad (11)$$

with

$$w_{i11} = (\mathbf{r}_i - \mathbf{s}_{i1})^T (\mathbf{e}_{i2} \times \mathbf{e}_{i1}) \quad (12)$$

$$w_{i32} = \left(1 + \frac{l_{i7}}{l_{i3}}\right) \mathbf{s}_{i5}^T (\mathbf{s}_{i2} \times \mathbf{e}_{i2}) \quad (13)$$

$$\mathbf{s}_{i3} = \mathbf{r}_i - \mathbf{s}_{i1} - \mathbf{s}_{i2} \quad (14)$$

$$\mathbf{s}_{i5} = \mathbf{s}_{i2} + \mathbf{s}_{i7} - \mathbf{s}_{i6}. \quad (15)$$

Finally, matrix \mathbf{M}_i can be written as

$$\mathbf{M}_i = \mathbf{J}_i^{-1} \mathbf{W}_i, \quad i = 1, 2, 3. \quad (16)$$

An explicit expression for \mathbf{J}_i^{-1} is given in Appendix A.

To assemble the kinematics of the global robot, it is now possible to combine (3), (5), and (7) to obtain

$$\begin{bmatrix} \mathbf{s}_{14}^T [(\mathbf{Qd}_1) \times \mathbf{s}_{14}]^T \\ \mathbf{s}_{24}^T [(\mathbf{Qd}_2) \times \mathbf{s}_{24}]^T \\ \mathbf{s}_{34}^T [(\mathbf{Qd}_3) \times \mathbf{s}_{34}]^T \end{bmatrix} \begin{bmatrix} \dot{\mathbf{p}} \\ \boldsymbol{\omega} \end{bmatrix} = \begin{bmatrix} \mathbf{k}_1^T & \mathbf{0}^T & \mathbf{0}^T \\ \mathbf{0}^T & \mathbf{k}_2^T & \mathbf{0}^T \\ \mathbf{0}^T & \mathbf{0}^T & \mathbf{k}_3^T \end{bmatrix} \dot{\boldsymbol{\theta}} \quad (17)$$

where $\mathbf{0}$ stands for the 3-D zero column vector, namely $\mathbf{0} = [0 \ 0 \ 0]^T$ and $\dot{\boldsymbol{\theta}} = [\dot{\theta}_1^T \ \dot{\theta}_2^T \ \dot{\theta}_3^T]^T$ is the vector containing the nine actuated joint velocities. Since vector \mathbf{k}_i is of dimension 3×1 , the first matrix appearing on the right-hand side of (17) is of dimension 3×9 . Equation (17) contains the three velocity equations obtained from the first set of geometric constraints given by (1).

The second set of geometric constraints, given by (2), is now considered. Similarly to the above derivation, the time derivative of (2) yields

$$\dot{\mathbf{n}}^T \mathbf{s}_{i4} + \mathbf{n}^T (\dot{\mathbf{p}} + \dot{\mathbf{Qd}}_i - \dot{\mathbf{r}}_i) = 0 \quad (18)$$

which can be rewritten as

$$\mathbf{s}_{i4}^T \dot{\mathbf{n}} + \mathbf{n}^T \dot{\mathbf{p}} + \mathbf{n}^T \dot{\mathbf{Qd}}_i = \mathbf{n}^T \dot{\mathbf{r}}_i \quad (19)$$

in which

$$\mathbf{n} = \mathbf{Q}[\mathbf{z}']_{O'} \quad (20)$$

where $[\mathbf{z}']_{O'} = [0 \ 0 \ 1]^T$ represents the \mathbf{z}' -axis and is expressed in the moving frame, and

$$\dot{\mathbf{n}} = \dot{\mathbf{Q}}[\mathbf{z}']_{O'} = \boldsymbol{\Omega} \mathbf{n}. \quad (21)$$

With a derivation similar to the one given in (5), and using (21), the first term in (19) can be rewritten as

$$\mathbf{s}_{i4}^T \dot{\mathbf{n}} = (\mathbf{n} \times \mathbf{s}_{i4})^T \boldsymbol{\omega} \quad (22)$$

and the third term in (19) can be rewritten as

$$\mathbf{n}^T \dot{\mathbf{Qd}}_i = [(\mathbf{Qd}_i) \times \mathbf{n}]^T \boldsymbol{\omega}. \quad (23)$$

Adding (22) and (23) then yields

$$(\mathbf{n} \times \mathbf{s}_{i4})^T \boldsymbol{\omega} + [(\mathbf{Qd}_i) \times \mathbf{n}]^T \boldsymbol{\omega} = [(\mathbf{Qd}_i - \mathbf{s}_{i4}) \times \mathbf{n}]^T \boldsymbol{\omega}. \quad (24)$$

Now let

$$\mathbf{c}_i = \mathbf{Qd}_i - \mathbf{s}_{i4} \quad (25)$$

which is the vector from point O' to the center of joint S_i . Then, (19) can be rewritten as

$$\mathbf{n}^T \dot{\mathbf{p}} + (\mathbf{c}_i \times \mathbf{n})^T \boldsymbol{\omega} = \mathbf{n}^T \dot{\mathbf{r}}_i \quad (26)$$

in which

$$\mathbf{n}^T \dot{\mathbf{r}}_i = \mathbf{n}^T (\mathbf{M}_i \dot{\boldsymbol{\theta}}_i) = \mathbf{k}_{i+3}^T \dot{\boldsymbol{\theta}}_i, \quad i = 1, 2, 3 \quad (27)$$

where \mathbf{M}_i is defined in (16) and

$$\mathbf{k}_{i+3}^T = \mathbf{n}^T \mathbf{M}_i \quad (28)$$

is a line vector of dimension 1×3 . Rewriting (26) in matrix form, we obtain

$$\begin{bmatrix} \mathbf{n}^T (\mathbf{c}_1 \times \mathbf{n})^T \\ \mathbf{n}^T (\mathbf{c}_2 \times \mathbf{n})^T \\ \mathbf{n}^T (\mathbf{c}_3 \times \mathbf{n})^T \end{bmatrix} \begin{bmatrix} \dot{\mathbf{p}} \\ \boldsymbol{\omega} \end{bmatrix} = \begin{bmatrix} \mathbf{k}_4^T & \mathbf{0}^T & \mathbf{0}^T \\ \mathbf{0}^T & \mathbf{k}_5^T & \mathbf{0}^T \\ \mathbf{0}^T & \mathbf{0}^T & \mathbf{k}_6^T \end{bmatrix} \dot{\boldsymbol{\theta}}. \quad (29)$$

Equation (29) contains the three velocity equations obtained from the second set of constraints given by (2).

Finally, combining (17) and (29) and rearranging the components, we obtain

$$\mathbf{J} \mathbf{t} = \mathbf{K} \dot{\boldsymbol{\theta}} \quad (30)$$

where $\mathbf{t} = [\dot{\mathbf{p}}^T \ \boldsymbol{\omega}^T]^T$ is the vector of Cartesian velocities of the platform, and matrices \mathbf{J} and \mathbf{K} are written as

$$\mathbf{J} = \begin{bmatrix} \mathbf{s}_{14}^T [(\mathbf{Qd}_1) \times \mathbf{s}_{14}]^T \\ \mathbf{n}^T (\mathbf{c}_1 \times \mathbf{n})^T \\ \mathbf{s}_{24}^T [(\mathbf{Qd}_2) \times \mathbf{s}_{24}]^T \\ \mathbf{n}^T (\mathbf{c}_2 \times \mathbf{n})^T \\ \mathbf{s}_{34}^T [(\mathbf{Qd}_3) \times \mathbf{s}_{34}]^T \\ \mathbf{n}^T (\mathbf{c}_3 \times \mathbf{n})^T \end{bmatrix} \quad (31)$$

$$\mathbf{K} = \begin{bmatrix} \mathbf{k}_1^T & \mathbf{0}^T & \mathbf{0}^T \\ \mathbf{k}_4^T & \mathbf{0}^T & \mathbf{0}^T \\ \mathbf{0}^T & \mathbf{k}_2^T & \mathbf{0}^T \\ \mathbf{0}^T & \mathbf{k}_5^T & \mathbf{0}^T \\ \mathbf{0}^T & \mathbf{0}^T & \mathbf{k}_3^T \\ \mathbf{0}^T & \mathbf{0}^T & \mathbf{k}_6^T \end{bmatrix} \quad (32)$$

where, as mentioned above, $\mathbf{0}$ stands for a zero column vector of dimension 3×1 . Equation (30) represents the velocity equation

of the (6+3)-DOF kinematically redundant robot. It can be observed that matrix \mathbf{J} is of dimension 6×6 , while matrix \mathbf{K} is of dimension 6×9 . The dimensions of the matrices reflect the redundancy of the mechanism, which has, in fact, nine DOFs and nine actuators.

IV. SINGULARITY ANALYSIS

One of the main reasons for the limited orientational workspace of spatial parallel robots is the occurrence of singularities. Moreover, the translational workspace can always be increased by scaling up the robot, but this operation has no impact on the orientational workspace. Therefore, the singularity analysis is a very important component of the assessment of the performances of parallel robots. In this section, it will be shown that the singular configurations of the proposed redundant hybrid parallel robot are easily avoided, which yields an orientational workspace that is much larger than that of typical parallel mechanisms.

The singularities of the proposed robot architecture can be divided into two categories, namely the singularities (serial and parallel) occurring in one of the legs and the parallel (type II) singularities of the platform [18]–[21]. Since the legs include a serial and a parallel component, the singularities occurring in one of the legs can be of either type. However, because of the simple architecture of the legs—one revolute joint in series with a planar five-bar linkage—the analysis of the singularities occurring in a leg is rather straightforward. The type I (serial) singularities of a leg occur when matrix \mathbf{W}_i , defined in (11), is singular. Such a singularity occurs if the spherical joint is located on the axis of the first revolute joint. In this case, one has $w_{i11} = 0$ which makes matrix \mathbf{W}_i singular. This is avoided in the final design by making the first joint horizontal, i.e., $\alpha = \pi$, which renders this configuration unreachable. A type I singularity also occurs if \mathbf{s}_{i3} is orthogonal to $(\mathbf{e}_{i2} \times \mathbf{s}_{i2})$ or if \mathbf{s}_{i5} is orthogonal to $(\mathbf{e}_{i3} \times \mathbf{s}_{i6})$. It is rather straightforward to avoid such configurations by a proper dimensioning of the five-bar linkage to make these configurations correspond to the limits of the workspace. The type II (parallel) singularities that can occur in a leg correspond to a singularity of matrix \mathbf{J}_i , defined in (10). In this matrix, the first row is always orthogonal to the last two. Therefore, singularities can occur if the last two rows become linearly dependent. From the structure of the matrix, it is easy to see that this condition corresponds to the alignment of links $i5$ and $i7$. These configurations are easily avoided in practice. In summary, the possible singularities of the legs are easily handled.

Our attention is now turned to the singular configurations of the moving platform (parallel singularities of the robot), which are typically the most limitative for parallel or hybrid robots. Indeed, such singularities greatly limit the orientational workspace of spatial parallel mechanisms like the Gough–Stewart platform. The type II (parallel) singularities occur when $\det(\mathbf{J}) = 0$, where \mathbf{J} is the Jacobian matrix defined in (31). A geometric approach is used here to analyze these singularities. It is observed that, in the proposed mechanism, the spherical joint S_i is followed by link $i4$ and a revolute joint attached to the platform. With

such an arrangement, we can always find two lines expressed by Plücker coordinates corresponding to the constraints on the platform provided by each leg: One of them is parallel to the unit vector \mathbf{n} , while the other is along vector \mathbf{s}_{i4} , as shown in Fig. 2 (dashed lines). This appears very clearly in (31). In each leg, these two lines intersect at the center of joint S_i and they are perpendicular to each other. The Jacobian matrix \mathbf{J} defined in (30) is simply the combination of these six Plücker lines. By introducing GLG, the singular conditions of the mechanism can be determined geometrically. Indeed, this approach is very appropriate here because it does not require any computation and it allows a simple and exhaustive analysis.

In order to simplify the singularity analysis, we can divide the six lines into two sets and we show that we can investigate them independently. The first set contains the three lines parallel to unit vectors \mathbf{n} and the other set is formed by the three lines along vectors \mathbf{s}_{i4} . It can be observed, from Fig. 2, that the three lines along \mathbf{n} are parallel to each other in space, while the three lines along \mathbf{s}_{i4} are coplanar. The rationality to divide these six Plücker lines in two groups can be proved mathematically. Assume that the lines are expressed in an arbitrary frame whose origin is located on the plane formed by vectors \mathbf{s}_{i4} and whose z -axis is in the direction of the three unit vectors \mathbf{n} . If the Plücker coordinates of the lines expressed in this frame are noted $[b_j \ m_j \ n_j; \ p_j \ q_j \ w_j], j = 1, \dots, 6$, then the Plücker coordinates of the lines belonging to set one can be written as

$$\mathbf{J}_n = \begin{bmatrix} 0 & 0 & 1 & p_1 & q_1 & 0 \\ 0 & 0 & 1 & p_2 & q_2 & 0 \\ 0 & 0 & 1 & p_3 & q_3 & 0 \end{bmatrix} \quad (33)$$

while the Plücker coordinates of the lines belonging to set two can be expressed as

$$\mathbf{J}_a = \begin{bmatrix} b_4 & m_4 & 0 & 0 & 0 & w_4 \\ b_5 & m_5 & 0 & 0 & 0 & w_5 \\ b_6 & m_6 & 0 & 0 & 0 & w_6 \end{bmatrix}. \quad (34)$$

As mentioned above, these lines are represented as dashed lines going through joint S_i in Fig. 2. It can be observed that each line in matrix \mathbf{J}_n is linearly independent from the lines in matrix \mathbf{J}_a and vice versa. Therefore, it suffices to analyze each of the sets independently in order to determine the singular configurations. According to GLG, the largest number of linearly independent lines for spatial parallel lines or for coplanar lines—which is the case for each of the two sets here—is three. For any one of the two sets, a singularity may occur when the three lines intersect at one point or when they are parallel to each other on a plane. However, such singularities are easily avoidable for the proposed robot, as explained in the following sections.

A. Singularity of Set One

In this case, the i th line ($i = 1, 2, 3$) parallel to \mathbf{n} passes through point S_i and is restricted to rotate around the axis of the i th revolute joint attached to the platform. Its possible locations form the contour of a cylinder of radius equal to l_{i4} . We, therefore, have three cylinders with parallel axes. Singularities may occur when the three lines, one on each cylinder,

become coplanar. A simple way to avoid this possibility is to make the links $i4$ relatively short with respect to the platform in order to ensure that the cylinders are sufficiently far from one another, i.e., to ensure that no straight line can go through all three cylinders. This is easily taken care of at the design stage. For example, if the platform is an equilateral triangle with a circumradius R_p , one should have

$$l_{i4} < \frac{3}{4}R_p \quad (35)$$

in order to prevent such singularities.

B. Singularity of Set Two

Here, for this set of lines, the advantages of using kinematically redundant legs are reflected most vividly. A type II singularity occurs when the three coplanar Plücker lines belonging to this set intersect at a common point or are parallel to each other. However, such singular configurations can be avoided by reorienting one or two of the three links $i4$, using the kinematic redundancy, without changing the configuration of the platform. Moreover, it should be noted that although, in principle, using only two redundant legs is sufficient to avoid this set of singularities, we use three such that an analytical inverse kinematic solution can be obtained, which makes it possible to actively control the redundant coordinates, $\beta_i, i = 1, 2, 3$ (see Fig. 2), to keep the platform far away from type II singularities. This approach will be explained in the next section.

As a comparison, consider the nonredundant robot developed in [15], which is akin to the robot proposed in this article. In the nonredundant robot presented in [15], the six Plücker lines are associated with the six actuated input angles. For a given pose (position and orientation) of the platform, their directions cannot be changed, which yields unavoidable type II singularities. By contrast, in the redundant mechanism proposed here, the directions of the lines can be changed using the redundancy without affecting the pose of the platform. Except for the leg singularities, the present mechanism has only two different kinds of type II singularities and both of these are easily avoidable, as discussed above. However, for the nonredundant counterpart, five different kinds of singularities must be considered and no effective approach can be used to avoid them. The workspace—especially the orientational workspace—is considerably limited compared to that of the redundant mechanism proposed here. As an illustration of the capabilities of the proposed robot, its orientational workspace is shown in Section VII (Fig. 4) for the reference position, considering all possible leg and platform interferences. It can be readily observed that the robot is capable of very large tilt angles, which are far beyond the capabilities of other similar nonredundant parallel mechanisms. It should also be pointed out that the passive spherical joints S_i must have very large motion ranges to accommodate this motion. Such joints have been developed in [22] and are hence available.

V. INVERSE KINEMATICS

The inverse kinematics of most redundant manipulators is solvable only using numerical methods, which is achieved at the

velocity level [23]. For the hybrid robot proposed here, an analytical solution to the inverse kinematics which is straightforward, consistent, and conservative—thus overcoming the repeatability problem—can be obtained. Indeed, as explained in the singularity analysis presented above, it is possible to assign values to the angles β_i (see Fig. 2), which represent the redundant DOF, independently from the platform pose. For example, angles β_i can be prescribed to remain constant at all times in order to generate a configuration that always remains far away from singularities. Other means of determining the redundant angles β_i can also be implemented, as it will be shown in an upcoming section.

Therefore, for a given pose of the platform (vector \mathbf{p} and matrix \mathbf{Q}) and with given values of angles $\beta_i, i = 1, 2, 3$, the position of the spherical joint, vector \mathbf{r}_i , in each of the legs is readily computed as

$$\mathbf{r}_i = \mathbf{p} + \mathbf{Q}\mathbf{d}_i - \mathbf{s}_{i4}, \quad i = 1, 2, 3. \quad (36)$$

Once these vectors are obtained, each of the legs can be considered as a 3-DOF robot that is used to position the spherical joint and an analytical solution of the inverse kinematics is readily obtained for such a robot. Due to the five-bar linkages in the legs, this problem admits at most eight solutions and the branches of solution are easily determined. The detailed equations are straightforward and are given in Appendix B. These equations are used to determine the workspace and other characteristics of the robot.

As a comparison, consider the (6+3)-DOF redundant parallel robot proposed in [13]. It was shown that all singularities can be avoided for this robot by exploiting the redundancy. However, the redundancy resolution must be computed numerically and the conservative nature of the solution cannot be guaranteed. By contrast, the redundancy resolution of the robot proposed here is straightforward and conservative while requiring almost no computations.

VI. FORWARD KINEMATICS

When all actuator coordinates are prescribed, the position of each spherical joint is readily obtained by solving the forward kinematics of each of the legs. The solution of this problem is straightforward and leads to two solutions in each leg because of the five-bar linkage arrangement. Also, the robot is designed to always operate in one of these two solutions and a unique solution is readily determined. Once the positions of the three spherical joints are obtained, the position and orientation of the moving platform can be computed using the same formulation as for planar 3-DOF parallel manipulators [24], applied in the plane formed by the three spherical joints. This formulation yields a sixth-order polynomial equation. Nevertheless, it should be pointed out that, in practice, a numerical solution is used because of its computational efficiency and to avoid having to select the proper polynomial root. Also, because the robot configuration is always far from singularities and because an initial guess close to the solution is available, the numerical procedure converges stably and quickly. A comprehensive discussion on the forward kinematic problem of the proposed robot is given in [25], in

which several other approaches were proposed and where it was shown that the forward kinematic problem of this robot is significantly simpler than that of other kinematically redundant parallel robots, such as the one proposed in [13].

VII. WORKSPACE

For illustrative purposes, the geometric parameters used for the workspace evaluation of the proposed robot are chosen as follows:

$$\begin{aligned} R_b &= 250 \text{ mm}, \quad R_p = 125 \text{ mm}, \quad l_{ei1} = l_{i4} = 50 \text{ mm} \\ l_{i6} &= l_{i7} = 150 \text{ mm}, \quad l_{i2} = l_{i3} = l_{i5} = 300 \text{ mm}, \\ \alpha &= 120^\circ, \quad \beta_i = 97^\circ, \quad i = 1, 2, 3 \end{aligned}$$

where R_b and R_p are, respectively, the circumradius of the base and platform, l_{ei1} is the length of link $i1$ of the i th leg, and angles β_i are chosen such that the robot will never be in a type II singular configuration. The geometric parameters of the robot are chosen based on a design exercise with the consideration that the size of the prototype be suitable and convenient for pHRI. The analytical inverse kinematic solution is exploited for planning the motions of the robot and a discretization method is implemented in the evaluations.

A. Translational Workspace

In this evaluation, the orientation of the platform is $\mathbf{Q} = \mathbf{I}$, where \mathbf{I} is the 3×3 identity matrix. The base of the mechanism is regarded as the lower boundary of the workspace. In order to prevent the type I singularities, the minimal perpendicular distance between the center of the i th spherical joint and the axis of the corresponding first actuated revolute joint is set to be 20 mm, and the range of the angle between vectors \mathbf{s}_{i2} and \mathbf{s}_{i7} (see Fig. 2) is limited to be $[10^\circ, 170^\circ]$. Each link of the robot is modelled as a cylinder with a radius of 7.5 mm. A safety distance d between each pair of not directly connected cylinders is set to $d = 5$ mm. A mechanical interference occurs when $d < 5$ mm. The position of the platform during the evaluation is given as

$$\mathbf{p} = \begin{bmatrix} d_p \cos \theta_c & d_p \sin \theta_c & h \end{bmatrix}^T \quad (37)$$

with

$$0 \leq d_p \leq d_{p,\max}, \quad 0 \leq \theta_c \leq 2\pi, \quad \text{and} \quad 0 \leq h \leq h_{\max} \quad (38)$$

where d_p is the distance between the configuration of the platform and the reference configuration in the x - y plane, in a direction defined by angle θ_c , and h is the height (along the z -axis of the base frame) of the platform. The simulation intervals of d_p and h , and of θ_c , are set to 1 mm and 1° , respectively. These intervals, as well as those set for assessing the orientational workspace in the next section, are chosen based on the compromise between the calculation time and accuracy of the obtained workspace. The platform reaches a boundary of the workspace ($d_p = d_{p,\max}$ or $h = h_{\max}$) if passive spherical joint limits or mechanical interferences are detected.

The evaluation is conducted in two steps. First, we determine the upper boundary of the workspace, h_{\max} , by setting $d_p = 0$

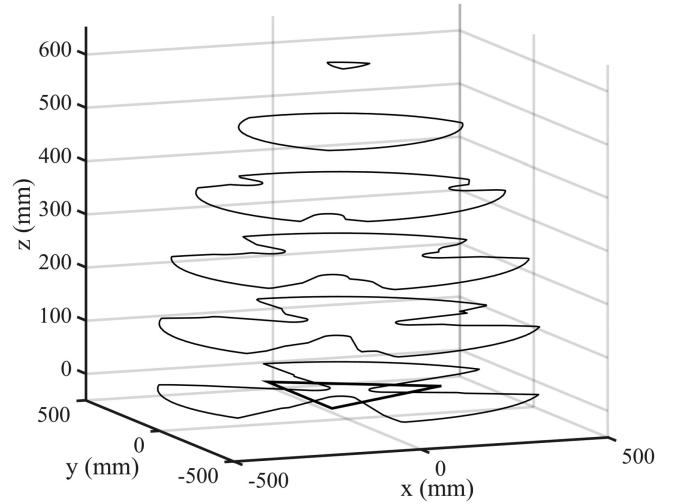


Fig. 3. Some layers of the translational workspace of the proposed architecture. The triangle at the base represents the footprint of the robot, i.e., the triangle defined by the three points (one in each leg), each corresponding to the intersection of the axes of the three actuators of a given leg.

and $\theta_c = 0$. Then, for each layer of h , the $d_{p,\max}$ is determined by moving the platform in the direction defined by each value of θ_c . In addition, we assume that the novel 4-R 4-DOF spherical joint (a Hooke joint with two additional R joints) proposed in [22] is used instead of the common 3-R joint (a Hooke joint with an extra R joint). Since the additional revolute joint in the 4-R joint allows the self motion of the Hooke joint, the 4-R spherical joint can generate a large motion range of $\pm 150^\circ$. In fact, the 4-DOF spherical joints proposed in [22] are used in the prototype of the proposed robot.

The results of the workspace evaluation are presented in Fig. 3 where some layers of the translational workspace are shown and where the triangle at the base represents the footprint of the robot. The robot is singularity-free throughout the translational workspace. However, due to the type I singularity condition (one), the lower part of the workspace is limited. As mentioned, this limitation can be improved by increasing the angle α . Indeed, if $\alpha = \pi$, the translational workspace will be convex, which is a desirable property for parallel mechanisms. In fact, $\alpha = \pi$ is chosen in the prototype described in an upcoming section. Also, as a comparison, for the nonredundant counterpart of the proposed robot [16], the translational workspace might be split into different regions due to singularities.

B. Orientational Workspace

The orientational workspace was evaluated when the position of the platform is fixed at $\mathbf{p} = [0 \ 0 \ 350]^T$ mm. Type I singularities are completely excluded in this location. Thereby, the orientational workspace is limited only by the passive spherical joint limits and mechanical interferences.

Tilt and torsion angles are used to illustrate the orientational workspace [26]. The result is shown in Fig. 4. Cylindrical coordinates (z, r, θ_c) are used in this representation, where the z -axis stands for the torsion angle (ψ), the radius r stands for

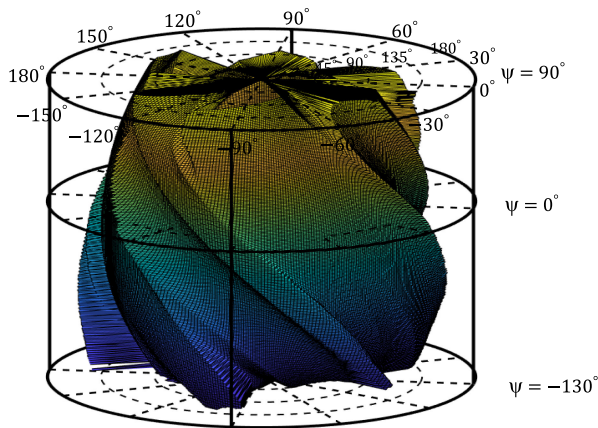


Fig. 4. Orientational workspace of the proposed architecture in the reference position.

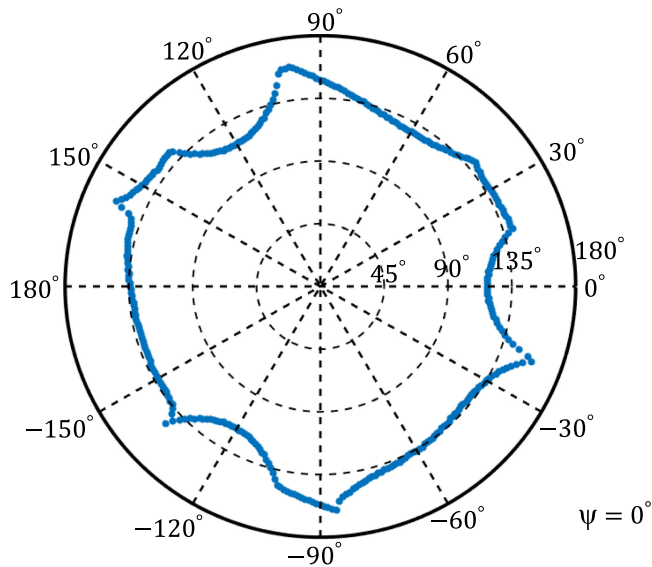


Fig. 5. Largest tilt angles of a section (zero torsion) of the proposed architecture.

the tilt angle, and θ_c is the angle defining the axis of the tilt rotation. It can be seen that a large span of the torsion angle (220°) can be reached. In Fig. 5, a section of the workspace corresponding to zero torsion is presented. It can be observed that the platform can reach a very large tilt angle of more than $\pm 135^\circ$ in certain directions. In the worst directions, the tilt angles can still be much larger than 90° . These results clearly show that the platform can produce an excellent rotational performance. By contrast, due to singularities, the maximum tilt angle of a Gough–Stewart platform in most cases is approximately 45° , and it is approximately 40° for the nonredundant counterpart of the proposed robot [16].

VIII. UTILISING THE REDUNDANCY TO OPERATE A GRIPPER

In Section IV, it was shown that it is easy to avoid all type II singularities of the proposed robot by proper design and very simple trajectory planning. As an extra benefit of the

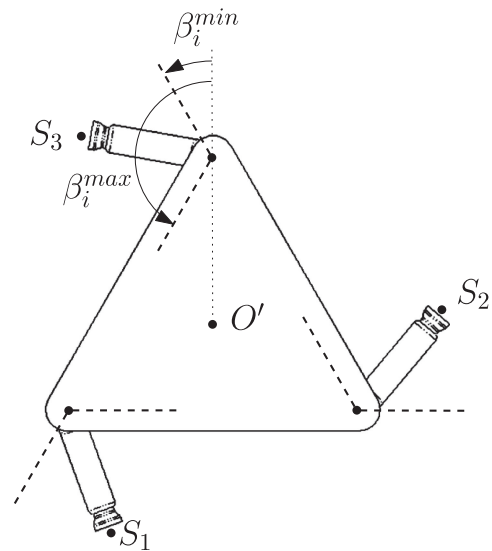


Fig. 6. Ranges of orientation of the distal links (domains for β_i) where singularity avoidance is guaranteed: $\beta_i \in]30^\circ, 150^\circ[$, $i = 1, 2, 3$.

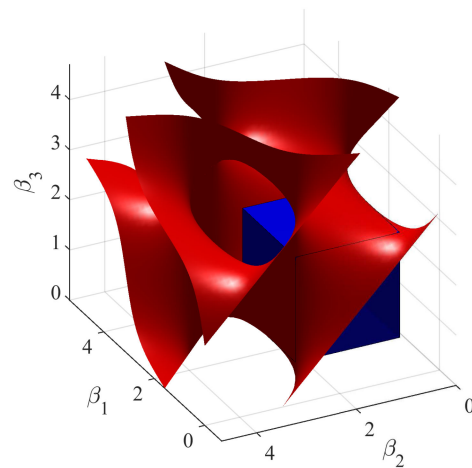


Fig. 7. Singularity locus of the proposed robot. The unit of β_i , $i = 1, 2, 3$ in this figure is radian. It is noted that this singularity locus is defined in the space of the redundant degrees of freedom and is independent from the position and orientation of platform. The box shown in blue represents the singularity-free zone corresponding to the inequalities given in (39).

proposed architecture, the redundancy of the robot can be further exploited, for instance, to operate a gripper from the base motors, similarly to what was proposed in [27] for SCARA-type robots. Indeed, in the above, the redundancy was used to avoid singular configurations, which leaves infinitely many nonsingular configurations for a given position and orientation of the platform. Considering again the platform and the links $i4$, it can be readily observed, as shown in Fig. 6, that if links $i4$ are maintained at an angle comprised within the ranges illustrated, namely $\beta_i \in]\beta_i^{\min}, \beta_i^{\max}[=]30^\circ, 150^\circ[$, then type II singularities can never occur (the three lines can never become dependent). This is also confirmed by the singularity locus, plotted in the $[\beta_1, \beta_2, \beta_3]$ space in Fig. 7. Indeed, it can readily be determined, from this

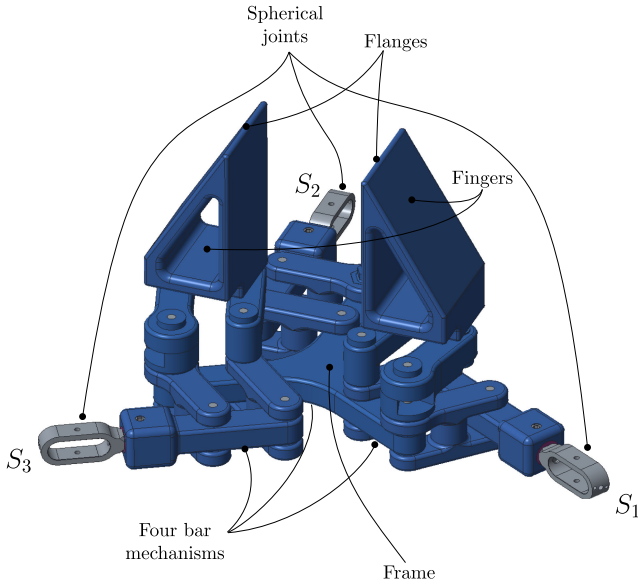


Fig. 8. Mechanical arrangement of the platform and gripper.

graph, that a box defined as

$$30^\circ < \beta_i < 150^\circ, i = 1, 2, 3 \quad (39)$$

is free from singularities. This box is shown in blue in Fig. 7.

In order to exploit the singularity-free ranges of motion determined above, the platform and links $i4$ of the robot are modified so that two of the degrees of redundancy are used to operate a gripper by changing angle β_i . To this end, the revolute joints at the platform are replaced with planar parallelogram four-bar linkages. The resulting mechanism is shown in Fig. 8. The fingers of the gripper are mounted on two of these mechanisms. The proximal links of the mechanisms have the same length so that the fingers follow a circular path while keeping the same orientation. The shape of the platform allows a symmetric parallel movement of the fingers, which can each be controlled independently. Fig. 9 illustrates the kinematics of the gripper linkages. It can be observed that it is possible to define virtual revolute joints with respect to which the spherical joints S_i rotate. These virtual joints correspond to the revolute joints attached to the platform in the original architecture. Two of the parallelogram mechanisms are modified so that two of the degrees of redundancy are used to operate the jaws of a gripper. For each jaw, one of the proximal members is extended and two links are added to form a second parallelogram. Each extension comes with an angle in order to exploit the best range of motion for the virtual links and the mechanisms supporting the jaws. Indeed, in the mid-range configuration, angles β_i are at 90° and the proximal members of the second parallelogram are normal to the closing trajectory of the jaws. The jaws are fixed to the distal members of the second parallelogram mechanism, which allows to maintain the orientation of the jaws. The relations between the opening distances δ_1 and δ_3 and angles β_1 and β_3 can be

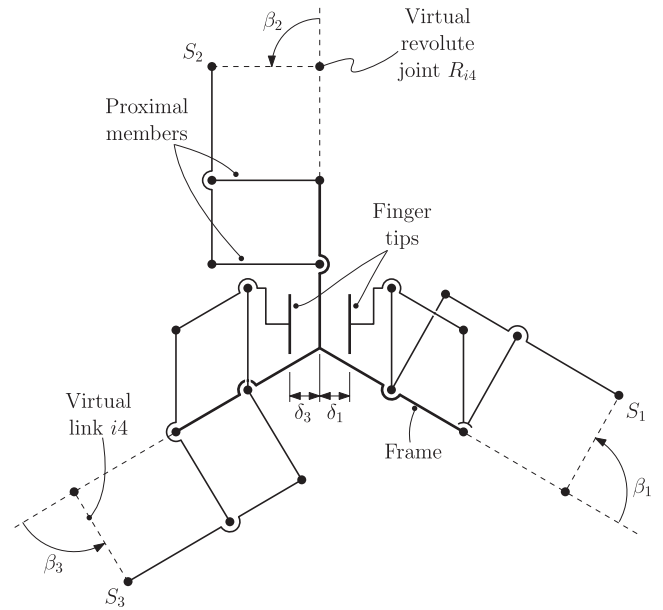


Fig. 9. Kinematics of the gripper linkages.

written as

$$\delta_1 = A \left(\frac{1}{2} + \cos \beta_1 \right), \quad \delta_3 = A \left(\frac{1}{2} - \cos \beta_3 \right) \quad (40)$$

where A is the maximum opening of the fingers (δ_1 and δ_3), which is equal to 25 mm in the current design. Because the fingers remain in the same orientation while moving, only the lateral distances between the flanges of the fingers and the center of the effector are considered to calculate the opening values δ_i , $i = 1, 3$. Using (40), it can be readily shown that the robot is kept well away from singularities when operating the gripper. Indeed, the design is such that when the fingers are closed ($\delta_1 = \delta_3 = 0$), one has $\beta_1 = 120^\circ$ and $\beta_3 = 60^\circ$ and when the fingers are completely open ($\delta_1 = \delta_3 = A$), one has $\beta_1 = 60^\circ$ and $\beta_3 = 120^\circ$. Angles β_i are mechanically limited to the range $[60^\circ, 120^\circ]$ and hence type II singularities are completely avoided.

The opening of the fingers of the gripper can then be included in the specification of the Cartesian coordinates of the robot. Angles β_i are then readily computed using (40). Hence, for a prescribed position and orientation of the platform as well as a prescribed opening of each of the fingers of the gripper—together with the orientation of the third link connected to the platform which is selected at mid-range of the corresponding angle β_i —the joint coordinates of the nine motors are readily computed using the procedure described in Section V.

IX. PROTOTYPING

A prototype of the proposed hybrid robot was designed and built. A Computer Aided Design (CAD) model of the prototype is shown in Fig. 10 and a photograph of the prototype is shown in Fig. 11. In the prototype, two of the redundant DOF are used to operate the jaws of a gripper, as described in the preceding section. The third redundant DOF is used to maintain angle β_i at

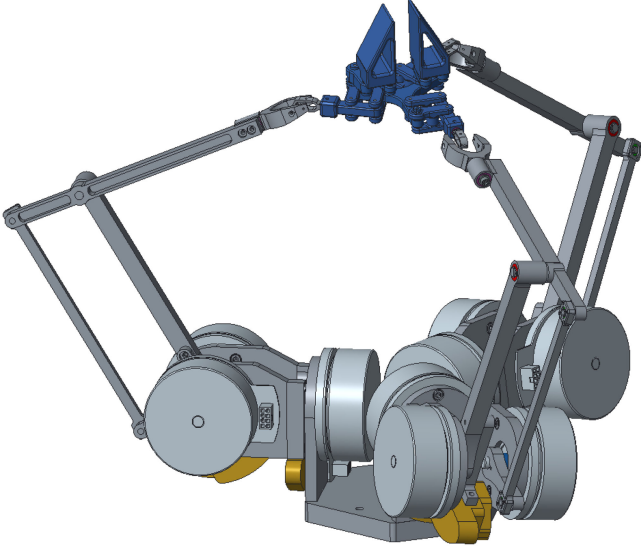


Fig. 10. CAD model of the proposed hybrid robot.

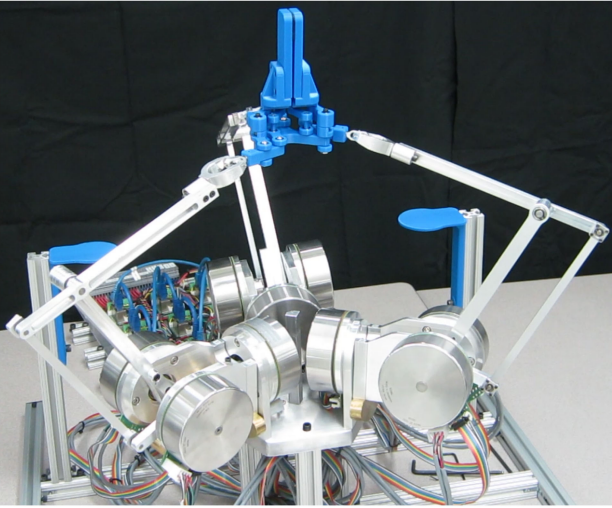


Fig. 11. Photograph of the prototype of the proposed hybrid robot.

a value that guarantees that the robot is far from type II singular configurations. Because singularities can always be avoided, the robot has a large workspace, especially in orientation. Rotations of $\pm 90^\circ$ can be performed around each of the Cartesian axes in a significant portion of the positioning workspace.

The actuators used are EC 90 flat, brushless, 260 W, from Maxon. They are equipped with encoders that provide a resolution of 16 384 counts per turn using quadrature. In order to ensure backdrivability, no mechanical transmissions are used, i.e., a direct drive arrangement is chosen. The total moving mass of the robot (including six of the nine actuators) is approximately 11.2 kg including 2.8 kg for the counterweights, which are used to minimize the static torques on the actuators. However, it should be noted that most of the moving mass of the robot is located very close to the base. Therefore, the inertia of the moving parts is very low due to the lightweight construction

of the legs and gripper and due to the fact that the gripper is operated from the motors located at the base (no actuator needs to be mounted on the end-effector to operate the gripper).

X. CONTROL

A. Position Control

A position controller is first implemented. As described above, the robot has nine DOFs. For a specified position and orientation of the end-effector, gripper opening and/or redundant angle β_i , the inverse kinematics are readily solved. The position controllers of each of the three legs of the robot can then be managed independently. A dynamic model of each of the legs was developed based on the Lagrangian formulation. In order to approximate the dynamic effect of the end-effector, a point mass of 1/3 of the mass of the end-effector is added at the tip of each leg. Although this is an approximation, it is sufficiently accurate for control purposes. The dynamic model of leg i (for $i = 1, 2, 3$) can be written as

$$\mathbf{M}_i(\boldsymbol{\theta}_i)\ddot{\boldsymbol{\theta}}_i + \mathbf{c}_i(\dot{\boldsymbol{\theta}}_i, \boldsymbol{\theta}_i) + \boldsymbol{\tau}_{gi}(\boldsymbol{\theta}_i) = \boldsymbol{\tau}_i \quad (41)$$

where \mathbf{M}_i is the generalized inertia matrix of leg i , \mathbf{c}_i is the vector of Coriolis and centrifugal forces, $\boldsymbol{\tau}_{gi}$ is the vector of joint gravitational torques, and $\boldsymbol{\tau}_i$ is the vector of joint torques. Since the velocity of the legs is not large, the vector of Coriolis and centrifugal forces and the other quadratic term are small compared to the inertial and gravity terms. Therefore, the dynamic model can be simplified to

$$\mathbf{M}_i(\boldsymbol{\theta}_i)\ddot{\boldsymbol{\theta}}_i + \boldsymbol{\tau}_{gi}(\boldsymbol{\theta}_i) = \boldsymbol{\tau}_i. \quad (42)$$

A computed torque method is then used to control the motion of the legs. The control torque vector $\boldsymbol{\tau}_{ci}$ can be written as

$$\boldsymbol{\tau}_{ci} = \mathbf{M}_i \left[\ddot{\boldsymbol{\theta}}_{di} + \mathbf{K}_{vi}(\dot{\boldsymbol{\theta}}_{di} - \dot{\boldsymbol{\theta}}_i) + \mathbf{K}_{pi}(\boldsymbol{\theta}_{di} - \boldsymbol{\theta}_i) \right] + \boldsymbol{\tau}_{gi} \quad (43)$$

where $\boldsymbol{\theta}_{di}$ is the vector of prescribed joint coordinates, which is readily obtained from the inverse kinematics and \mathbf{K}_{vi} and \mathbf{K}_{pi} are, respectively, the matrices of D and P gains. The corresponding control block diagram is shown in Fig. 12. The damping term appearing on the diagram is used only for the collaborative mode and will be described in the next paragraph.

B. Collaborative Mode

Collaborative robots include a control mode in which the robot can be guided manually by direct physical contact between the user and the robot. In the vast majority of collaborative robots, this mode of operation is based on admittance control using either a force/torque sensor mounted at the end-effector of the robot or joint torque sensors. Indeed, impedance control cannot be used because such robots are not backdrivable due to the gear transmissions mounted between the actuators and the robot joints. Although admittance control based on force/torque sensors is a functional approach, it greatly limits the bandwidth of the interaction between the human user and the robot and, therefore, makes the interaction less intuitive[2], [28]. In an impedance control scheme, the robot is moved by

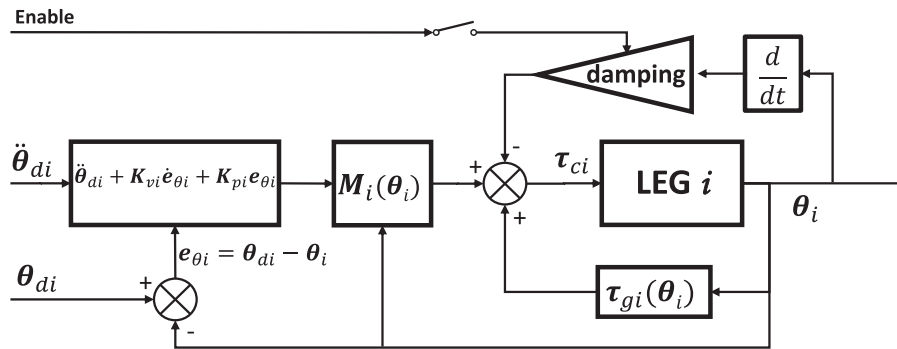


Fig. 12. Block diagram of the position controller of leg i of the robot.

the user. This motion is then perceived by the joint encoders and the actuators react with an appropriate torque, according to a desired dynamics [29]. Since the robot proposed in this article is mechanically backdrivable and the inertia of the moving parts is small, impedance control can be used, thereby greatly increasing the bandwidth of the human–robot interaction. A special case of impedance control is used here in which the impedance rendered at the end-effector is the actual mechanical impedance of the moving parts of the robot. Hence, there is no impedance model in the controller. The robot is moved by the user, who feels the real inertia of the robot. The leg controllers described in the preceding paragraph are then used to follow this motion. However, since the prescribed acceleration is not known—the trajectory is given by the user and inferring the acceleration from the joint encoders is too noisy—the inertia term in (43) is not used. Therefore, (43) simplifies to

$$\tau_{ci} = M_i \left[K_{vi}(\dot{\theta}_{di} - \dot{\theta}_i) + K_{pi}(\theta_{di} - \theta_i) \right] + \tau_{gi} \quad (44)$$

which means that the leg controller provides only gravity compensation and PD error feedback. As mentioned above, the user feels the moving inertia of the robot. However, the architecture of the robot is such that this inertia is small and falls within a very comfortable range for the user. The advantage of this approach, which is made possible by the architecture of the robot, is that the controller is extremely simple and therefore very robust. Also, no sensor is required (force/torque sensor, joint torque sensor, or other), not even the actuator current measurement.

If it is desired to render to the user an impedance that is different from the real impedance of the robot, the motor currents can be measured and used to infer the joint torques/accelerations. Indeed, since the actuators are directly coupled to the robot links (direct drive), the motor currents provide an accurate measure of the joint torques. An impedance model could then be used and the real inertia of the robot could be compensated using (43), yielding a standard impedance controller. This is not implemented in the current controller and is left for future work. The current controller aims at demonstrating the capability of the robot to produce a very intuitive interaction with a very simple sensorless control algorithm.

Another issue that must be addressed is the kinematic redundancy, which makes the direct application of an impedance

controller less straightforward. Indeed, since the proposed robot is kinematically redundant, infinitely many actuated joint configurations correspond to a given Cartesian pose (position and orientation) of the platform. Hence, if the user is free to move the end-effector of the robot, a strategy must be developed to ensure the proper joint motions of the robot. In the proposed robot, if the user is holding one body of the end-effector mechanism, six DOFs are prescribed. Similarly, an example is shown in Video-2 (Human–robot interaction), where the user holds both jaws of the gripper. In this case, the position and orientation of one body of the end-effector mechanism as well as the distance between the two jaws of the gripper are prescribed, for a total of seven DOFs that are then imposed by the user. The other two DOFs must be controlled. The resolution of the redundancy is included in the collaborative control mode, as described below.

The global control strategy used in this robot is represented schematically in Fig. 13 and can be described as follows. First, the motion imparted to the robot end-effector by the user constrains n -DOF ($n \geq 6$). For instance, as mentioned above, if the user holds both jaws of the gripper, the position and orientation of one body of the end-effector mechanism as well as the distance between the two fingers are constrained, yielding $n = 7$. Then, at each time step, the configuration of the robot due to the user input motion is determined based on the m actuated joint coordinates (here $m = 9$). Namely, using these m encoder values, the direct kinematics of the robot are solved in order to determine the pose of the platform and the three redundant DOFs. Given the pose of the platform and the gripper opening imposed by the user, the inverse kinematic problem is then solved to determine the proper configuration of the robot, i.e., the actuated joint configuration that matches the pose of the platform and the opening of the gripper (imposed by the user) and that drives the redundant DOF to a prescribed configuration that is far away from singularities. Using this approach, which involves successively solving the direct kinematics and the inverse kinematics, the robot follows the input of the user while always keeping a configuration that is free from singularities and far from mechanical limits. It is pointed out that the number of free variables that can be assigned by the algorithm in the inverse kinematic procedure is equal to $(m - n)$ (e.g., 2 in the example given above). Nevertheless, the robot will never approach singular configurations because the

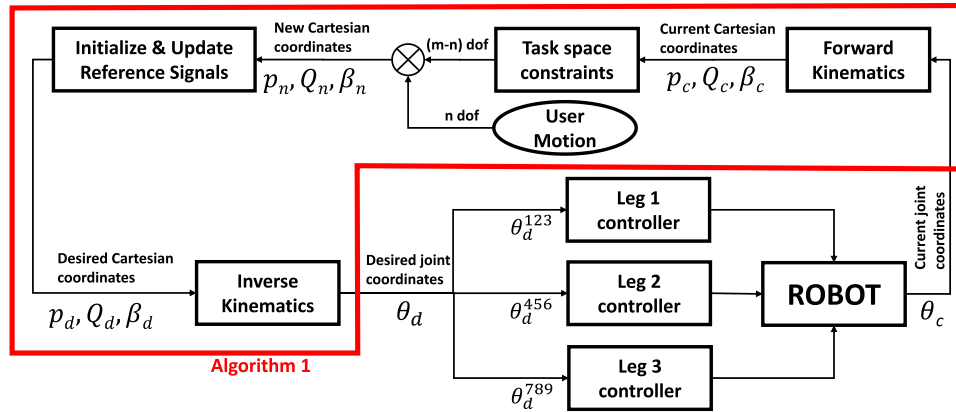


Fig. 13. Block diagram of the collaborative controller of the robot.

mechanical limits of the end-effector articulations prevent such configurations, as explained in Section VIII.

C. Transition Between Control Modes

In a practical application, the desired behaviour of the robot is that the user can move the end-effector as smoothly and freely as possible when physically interacting with it and that the end-effector remains in its current pose when the user lets go of it. In order to obtain this behavior, the controller must be able to switch from the position control mode to the collaborative mode and vice versa. This is implemented using a double threshold strategy. For each actuator of the robot, a velocity threshold is first defined in order to determine whether the user desires to move or to stop the interactive guidance. Moreover, a position error threshold is also defined so that the controller can distinguish between the initiation of a motion guidance by the user and the effect of other external forces such as gravity. A binary signal based on these thresholds is generated by each of the actuators to indicate the intention of the user. The robot then updates continuously n -DOFs, along with $(m - n)$ prescribed values, as long as one of these signals is active (collaborative mode). Otherwise, the controller stops updating the joint positions and reverts to position control to remain in the configuration in which the user left it. The position threshold is chosen based on the maximum position error of the motion controller in each leg. When the position error is larger than this threshold, the error is no longer considered a disturbance but rather a guidance command. On the other hand, the velocity threshold needs to be adjusted according to the operator movement, which defines the desired minimum velocity. As indicated in Figs. 12 and 13, a small damping is also added so that the motion is more natural for the user. Indeed, since there is very little friction in the robot and in the actuators, the user can impart very fast motions to the robot, which may not feel so natural. The damping term provides a feeling of additional stability and intuitiveness to the user. The damping term is enabled only in the collaborative mode since, in this mode, the position error is typically very small, which makes the PD terms very small in the controller. Also, virtual walls can be implemented, which limit the motion of the robot, thereby providing the illusion of sharp contacts with a virtual environment to the user. This feature can be useful

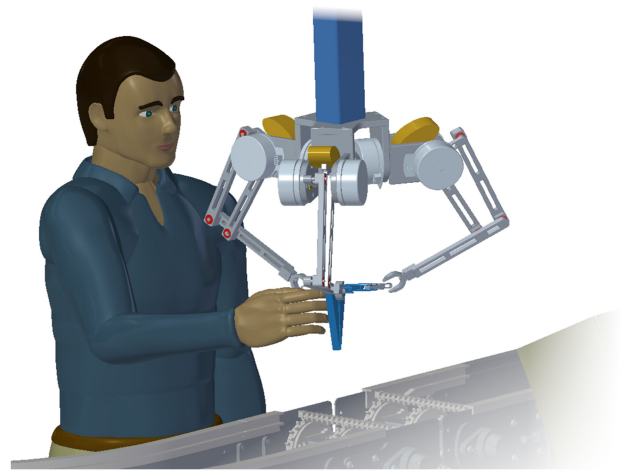


Fig. 14. Illustration of the intended use of the robot in an upside down configuration.

in haptic applications, as illustrated in Video-2 (Human–robot interaction). Finally, this control method can be summarized in the pseudocode given in Algorithm 1.

It should also be mentioned that a calibration jig was designed specifically for the robot. The jig is fixed to the base and it includes a peg that extends to the moving platform and whose special shape constrains all nine DOFs of the robot, in a reference configuration. The motor encoders corresponding to this configuration can then be read. The CAD model of the robot is used to verify the inverse kinematics in this configuration and then in other configurations, based on this reference, thereby allowing the calibration of the robot kinematics.

Finally, it should be pointed out that the robot is intended for use in the upside down configuration (and possibly mounted on a larger robot such as a gantry robot), as illustrated schematically in Fig. 14. In such a configuration, the end-effector's reference orientation is normal to the working surface, which maximizes the operational capabilities for grasping objects.

Algorithm 1: Collaborative Control Algorithm.

Input: vector current joint coordinates of legs 1, 2, and 3
Output: vector reference joint coordinates of legs 1, 2, and 3
Internal Variables: vector position (p), orientation (Q), vector roll-pitch-yaw angles ($ropy$) and vector redundant angles (β)
 $p_current, Q_current, \beta_current = forwardKinematics(input)$
if virtual wall is on **then**
 $p_new = p_current$ **AND** $conditions(p_current < virtualwall)$
 $ropy_current = matrix2ropy(Q_current)$
 $ropy_new = rpy_current$ **AND** $conditions(ropy < virtualwall)$
 $Q_new = rpy2matrix(ropy_new)$
end if
if singularity avoidance is on **then**
 $\beta_new = [\frac{\pi}{2}; \frac{\pi}{2}; \frac{\pi}{2}]$
end if
if user motion is detected **then**
 $output = inverseKinematics(p_new, Q_new, \beta_new)$
 $mode = User_guidance$
else
 $output = Previous_output$
 $mode = Position_control$
end if

XI. EXPERIMENTAL VALIDATION

In order to assess the physical interaction capabilities of the robot, a force-torque sensor is mounted on the end-effector, for measurement purposes. The force/torque sensor used in this experiment is an ATI-Mini40, which can measure the full six components of force/torque. The measurement is provided within a range ± 40 N in the x - and y -directions and ± 120 N in the z -direction. An Analog Data Acquisition (DAQ) card is used, which gives a resolution of $1/100$ N in the x - y -direction and of $1/50$ N in the z -direction. The update rate of this sensor can be set up to 28.5 kHz. Nonetheless, the controller is implemented using Simulink real-time and limitations of the other components only allow to operate the system at 2 kHz, or $T_s = 0.5$ ms.

A user physically interacts with the robot, which is controlled using the impedance control scheme described in Section X. It should be emphasized that the force/torque sensor is not used in the controller. It is used in this experiment only to measure the interaction forces between the user and the robot in order to assess the performance of the robot and of the proposed control scheme. In this experiment, the user imparts oscillating motion to the robot end-effector approximately in the x -, y -, and z -directions (successively). The Cartesian motion, computed from the measured joint displacements using the direct kinematics, is shown in Fig. 15. Based on the control scheme described in Section X, the direct kinematic problem is solved at each time

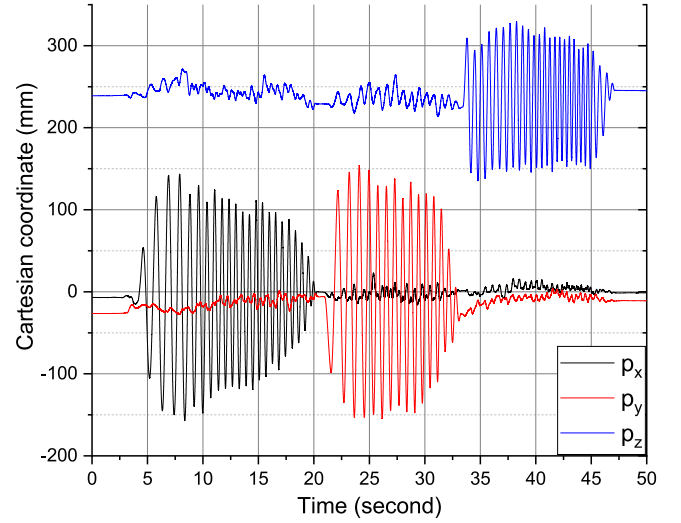


Fig. 15. Cartesian displacement of the end-effector during the interaction experiment.

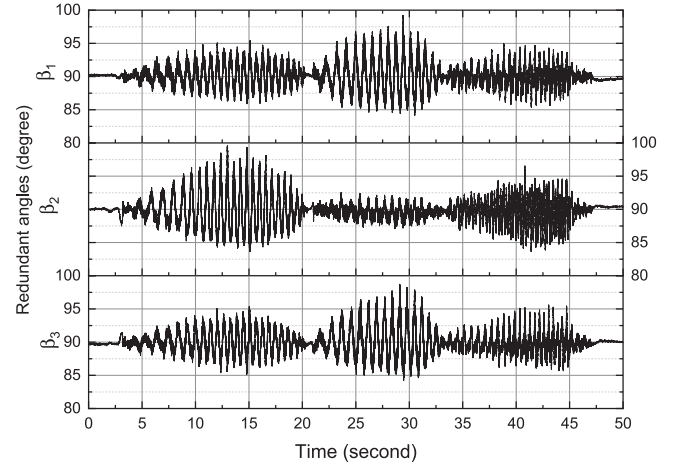


Fig. 16. Angles corresponding to the redundant DOFs ($\beta_i, i = 1, 2, 3$) during the interaction experiment.

step. The resulting redundant coordinates (angles β_i) remain close to the optimal value of 90° , as shown in Fig. 16.

The interaction forces between the user and the robot are measured throughout the experiment. The three force components are shown in Fig. 17. It can be observed from the displacements shown in Fig. 15 that the interaction involves oscillations of approximately ± 150 mm in the x - and y -directions and of ± 100 mm in the z -direction. With such amplitudes, it can be observed in Fig. 17 that the maximum forces that the user is applying are less than 6 N for the x and y motions and less than 8 N for the z motion. The small offset of force observed for the z motion is due to gravity. Indeed, the mass of the end-effector is not completely compensated by the counterweights included in the legs and by the gravity compensation terms in the controller. It can also be observed, from the graphs, that the oscillating motion is taking place at approximately 1.5 Hz for the x and y motions and at approximately 2.3 Hz for the

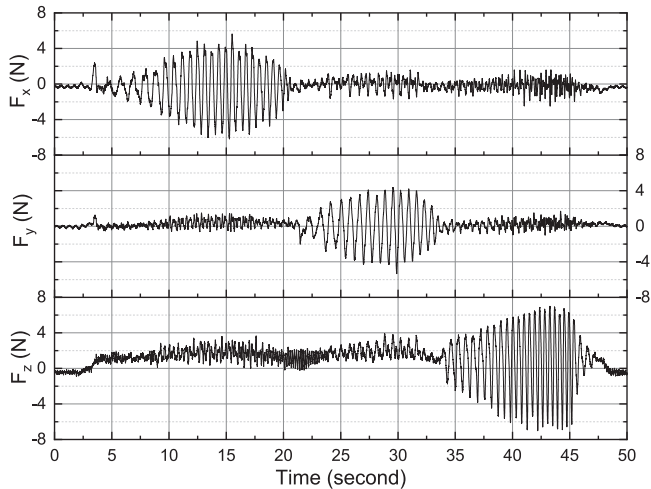


Fig. 17. Forces applied by the user to the robot during the interaction experiment.

vertical motion, which clearly demonstrates the high bandwidth of the interaction. The interaction frequencies are even higher for smaller amplitudes of motion. The perceived inertia can be computed from the results shown in Figs. 15 and 17. For the x - y motion, the perceived inertia is approximately 0.5 kg (acceleration of 10 m/s^2 and force of 5 N), while for the z motion, it is approximately 0.35 kg (acceleration of 20 m/s^2 and force of 7 N). As mentioned above, the control scheme is such that the mechanical inertia of the robot is felt by the user, meaning that the mechanical inertia is between 0.35 and 0.5 kg. Knowing that the total mass of the moving parts of the robot is 11.2 kg, it is clear that the fact that the mass is located mostly close to the base has a large impact on the inertia perceived by the user. Finally, neglecting the dynamics of the robot in the controller is justified by the approach that consists in rendering the real inertia of the robot to the user. Because of the design of the robot, this inertia falls within a comfortable range for the user. In future work, an impedance model could be included in the controller in order to modulate the impedance felt by the user. However, this is not necessary since the real impedance of the robot provides a very intuitive interaction. Indeed, as it can be observed in Video-2 (Human-robot interaction) accompanying this article, the interaction is very natural for the user due to the small moving inertia of the robot and its mechanical backdrivability.

XII. MULTIMEDIA MATERIAL

Two videos accompany this article. In the first video (Video-1 “Trajectory Control”), the architecture of the robot is presented, as well as its main characteristics. As indicated in the video, the maximum acceleration of the robot is approximately 25 m/s^2 in the vertical direction and 10 m/s^2 in the horizontal direction and the maximum angular acceleration is approximately 145 rad/s^2 . Because of the redundancy, the translational and rotational workspace of the robot is very large compared to other similar parallel mechanisms.

In the second video (Video-2 “Human-robot interaction”), the capability of the robot to produce a low-impedance high-bandwidth physical interaction with a human user is demonstrated. The possibility to use the robot as a haptic device (for example, by introducing virtual walls) is also demonstrated. Due to the low inertia of the mechanism, sharp contacts can be generated in this mode. The teaching and execution of a pick-and-place operation is then demonstrated.

XIII. CONCLUSION

In this article, a novel backdrivable (6+3)-DOF kinematically redundant hybrid parallel robot was introduced. It was shown that the type II singularities of the mechanism can be easily avoided by proper design and simple trajectory planning rules. As a result, the orientational workspace of the robot is very large when compared to other similar nonredundant parallel mechanisms. Moreover, although the architecture of the mechanism is not fully parallel, the moving actuators are located very close to the base and undergo motion with only a small amplitude, thereby greatly reducing the inertia of the moving components. In addition to avoiding singularities, it was shown that the kinematic redundancy can be used to operate a gripper mounted at the end-effector. This feature avoids the need to include an actuator on the end-effector in order to operate the gripper, which is another advantage regarding moving inertia. Indeed, any mass added to the end-effector is highly detrimental to the agility of a parallel robot. A prototype of the robot was built and demonstrated. A simplified impedance control scheme was implemented that exploits the backdrivability and low inertia of the robot. In this control scheme, the real physical impedance of the robot is rendered to the user. This simple control scheme does not require any force, torque, or current sensors while providing a high-bandwidth low-impedance interaction with a user, as demonstrated experimentally. The mechanical design of the robot makes it possible to use such a control scheme. The result is a dexterous robot that provides a very smooth and natural pHRI, as demonstrated in the accompanying videos. Future work includes mounting the robot in an upside down configuration on a gantry robot for the performance of typical industrial tasks requiring high dexterity and high bandwidth as well as the implementation of more advanced impedance control algorithms.

APPENDIX A

VELOCITY EQUATIONS OF THE $\underline{R}(\underline{R}\underline{R}\text{-}\underline{R}\underline{R}\underline{R})$ ROBOT LEG

Three constraint conditions can be determined for the $\underline{R}(\underline{R}\underline{R}\text{-}\underline{R}\underline{R}\underline{R})$ subleg contained in each $\underline{R}(\underline{R}\underline{R}\text{-}\underline{R}\underline{R}\underline{R})\text{SR}$ robot leg. First, \mathbf{e}_{i2} (or \mathbf{e}_{i3}), the direction vector of the actuated joint $i2$ (or $i3$), is perpendicular to the vector $(\mathbf{r}_i - \mathbf{s}_{i1})$ (see Fig. 2). Thus, we have

$$\mathbf{e}_{i2}^T (\mathbf{r}_i - \mathbf{s}_{i1}) = 0. \quad (\text{A.1})$$

Differentiating (A.1) with respect to time yields

$$\dot{\mathbf{e}}_{i2}^T (\mathbf{r}_i - \mathbf{s}_{i1}) + \mathbf{e}_{i2}^T \dot{\mathbf{r}}_i = 0 \quad (\text{A.2})$$

where it is noted that \mathbf{s}_{i1} is a constant vector in the proposed mechanism. Since

$$\dot{\mathbf{e}}_{i2} = \boldsymbol{\omega}_{i2} \times \mathbf{e}_{i2} = \dot{\theta}_{i1}(\mathbf{e}_{i1} \times \mathbf{e}_{i2}) \quad (\text{A.3})$$

then (A.2) can be rewritten as

$$\mathbf{e}_{i2}^T \dot{\mathbf{r}}_i = \dot{\theta}_{i1}(\mathbf{r}_i - \mathbf{s}_{i1})^T (\mathbf{e}_{i2} \times \mathbf{e}_{i1}). \quad (\text{A.4})$$

The second constraint equation can be written as

$$\mathbf{s}_{i3}^T \mathbf{s}_{i3} = (\mathbf{r}_i - \mathbf{s}_{i1} - \mathbf{s}_{i2})^T (\mathbf{r}_i - \mathbf{s}_{i1} - \mathbf{s}_{i2}) = l_{i3}^2 \quad (\text{A.5})$$

which can be rewritten as

$$(\mathbf{r}_i - \mathbf{s}_{i1})^T (\mathbf{r}_i - \mathbf{s}_{i1}) - 2(\mathbf{r}_i - \mathbf{s}_{i1})^T \mathbf{s}_{i2} = l_{i3}^2 - l_{i2}^2 \quad (\text{A.6})$$

in which

$$l_{i2}^2 = \mathbf{s}_{i2}^T \mathbf{s}_{i2}. \quad (\text{A.7})$$

Differentiating (A.6) with respect to time yields

$$(\mathbf{r}_i - \mathbf{s}_{i1})^T \dot{\mathbf{r}}_i - \mathbf{s}_{i2}^T \dot{\mathbf{r}}_i - (\mathbf{r}_i - \mathbf{s}_{i1})^T \dot{\mathbf{s}}_{i2} = 0 \quad (\text{A.8})$$

which can be rewritten as

$$(\mathbf{r}_i - \mathbf{s}_{i1} - \mathbf{s}_{i2})^T \dot{\mathbf{r}}_i = (\mathbf{r}_i - \mathbf{s}_{i1})^T \dot{\mathbf{s}}_{i2}. \quad (\text{A.9})$$

The time derivative of \mathbf{s}_{i2} can be written as

$$\dot{\mathbf{s}}_{i2} = \boldsymbol{\omega}_{si2} \times \mathbf{s}_{i2} = (\dot{\theta}_{i1} \mathbf{e}_{i1} + \dot{\theta}_{i2} \mathbf{e}_{i2}) \times \mathbf{s}_{i2}. \quad (\text{A.10})$$

Substituting (A.10) into (A.9) yields

$$\mathbf{s}_{i3}^T \dot{\mathbf{r}}_i = (\mathbf{r}_i - \mathbf{s}_{i1})^T [\dot{\theta}_{i1}(\mathbf{e}_{i1} \times \mathbf{s}_{i2}) + \dot{\theta}_{i2}(\mathbf{e}_{i2} \times \mathbf{s}_{i2})]. \quad (\text{A.11})$$

Since $(\mathbf{r}_i - \mathbf{s}_{i1})$, \mathbf{e}_{i1} , and \mathbf{s}_{i2} are coplanar, one can write

$$(\mathbf{r}_i - \mathbf{s}_{i1})^T (\mathbf{e}_{i1} \times \mathbf{s}_{i2}) = 0. \quad (\text{A.12})$$

Also

$$\begin{aligned} (\mathbf{r}_i - \mathbf{s}_{i1})^T (\mathbf{e}_{i2} \times \mathbf{s}_{i2}) &= (\mathbf{s}_{i3} + \mathbf{s}_{i2})^T (\mathbf{e}_{i2} \times \mathbf{s}_{i2}) \\ &= \mathbf{s}_{i3}^T (\mathbf{e}_{i2} \times \mathbf{s}_{i2}). \end{aligned} \quad (\text{A.13})$$

Hence, (A.11) can be rewritten as

$$\mathbf{s}_{i3}^T \dot{\mathbf{r}}_i = \dot{\theta}_{i2} \mathbf{s}_{i3}^T (\mathbf{e}_{i2} \times \mathbf{s}_{i2}). \quad (\text{A.14})$$

The third constraint equation can be written as

$$\mathbf{s}_{i5}^T \mathbf{s}_{i5} = (\mathbf{s}_{i2} + \mathbf{s}_{i7} - \mathbf{s}_{i6})^T (\mathbf{s}_{i2} + \mathbf{s}_{i7} - \mathbf{s}_{i6}) = l_{i5}^2 \quad (\text{A.15})$$

where

$$\mathbf{s}_{i7} = -\frac{l_{i7}}{l_{i3}} \mathbf{s}_{i3} = -\frac{l_{i7}}{l_{i3}} (\mathbf{r}_i - \mathbf{s}_{i1} - \mathbf{s}_{i2}). \quad (\text{A.16})$$

Differentiating (A.15) with respect to time yields

$$(\mathbf{s}_{i2} + \mathbf{s}_{i7} - \mathbf{s}_{i6})^T (\dot{\mathbf{s}}_{i2} + \dot{\mathbf{s}}_{i7} - \dot{\mathbf{s}}_{i6}) = 0 \quad (\text{A.17})$$

which can be rewritten as

$$\mathbf{s}_{i5}^T (\dot{\mathbf{s}}_{i2} + \dot{\mathbf{s}}_{i7}) = \mathbf{s}_{i5}^T \dot{\mathbf{s}}_{i6} \quad (\text{A.18})$$

where

$$\begin{aligned} \dot{\mathbf{s}}_{i2} + \dot{\mathbf{s}}_{i7} &= \dot{\mathbf{s}}_{i2} - \frac{l_{i7}}{l_{i3}} (\dot{\mathbf{r}}_i - \dot{\mathbf{s}}_{i2}) \\ &= \left(1 + \frac{l_{i7}}{l_{i3}}\right) \dot{\mathbf{s}}_{i2} - \frac{l_{i7}}{l_{i3}} \dot{\mathbf{r}}_i \end{aligned} \quad (\text{A.19})$$

and similarly to (A.10), $\dot{\mathbf{s}}_{i6}$ can be given as

$$\dot{\mathbf{s}}_{i6} = \boldsymbol{\omega}_{si6} \times \mathbf{s}_{i6} = (\dot{\theta}_{i1} \mathbf{e}_{i1} + \dot{\theta}_{i3} \mathbf{e}_{i3}) \times \mathbf{s}_{i6}. \quad (\text{A.20})$$

Substituting (A.19) and (A.20) into (A.18) then yields

$$\begin{aligned} \mathbf{s}_{i5}^T \left[\left(1 + \frac{l_{i7}}{l_{i3}}\right) (\dot{\theta}_{i1}(\mathbf{e}_{i1} \times \mathbf{s}_{i2}) + \dot{\theta}_{i2}(\mathbf{e}_{i2} \times \mathbf{s}_{i2})) - \frac{l_{i7}}{l_{i3}} \dot{\mathbf{r}}_i \right] \\ = \mathbf{s}_{i5}^T [\dot{\theta}_{i1}(\mathbf{e}_{i1} \times \mathbf{s}_{i6}) + \dot{\theta}_{i3}(\mathbf{e}_{i3} \times \mathbf{s}_{i6})]. \end{aligned} \quad (\text{A.21})$$

The above equation can be simplified to

$$-\frac{l_{i7}}{l_{i3}} \mathbf{s}_{i5}^T \dot{\mathbf{r}}_i = \dot{\theta}_{i2} \left(1 + \frac{l_{i7}}{l_{i3}}\right) \mathbf{s}_{i5}^T (\mathbf{s}_{i2} \times \mathbf{e}_{i2}) + \dot{\theta}_{i3} \mathbf{s}_{i5}^T (\mathbf{e}_{i3} \times \mathbf{s}_{i6}) \quad (\text{A.22})$$

since \mathbf{s}_{i5} is always perpendicular to $(\mathbf{e}_{i1} \times \mathbf{s}_{i2})$ and $(\mathbf{e}_{i1} \times \mathbf{s}_{i6})$.

Finally, the combination of (A.4), (A.14), and (A.22) gives

$$\mathbf{J}_i \dot{\mathbf{r}}_i = \mathbf{W}_i \dot{\boldsymbol{\theta}}_i \quad (\text{A.23})$$

where matrices \mathbf{J}_i and \mathbf{W}_i are, respectively, shown in (10) and (11). Finally, the Jacobian matrix of the $\underline{\mathbf{R}}(\underline{\mathbf{R}}\underline{\mathbf{R}}-\underline{\mathbf{R}}\underline{\mathbf{R}}\underline{\mathbf{R}})$ robot leg can be written as

$$\mathbf{M}_i = \mathbf{J}_i^{-1} \mathbf{W}_i \quad (\text{A.24})$$

where one has

$$\mathbf{J}_i^{-1} = \rho_i \left[(\mathbf{s}_{i3} \times \mathbf{s}_{i5}) - (\mathbf{e}_{i2} \times \mathbf{s}_{i5}) - \frac{l_{i3}}{l_{i7}} (\mathbf{e}_{i2} \times \mathbf{s}_{i3}) \right] \quad (\text{A.25})$$

with

$$\rho_i = \frac{1}{\mathbf{e}_{i2}^T (\mathbf{s}_{i3} \times \mathbf{s}_{i5})}. \quad (\text{A.26})$$

APPENDIX B

INVERSE KINEMATICS OF THE $\underline{\mathbf{R}}(\underline{\mathbf{R}}\underline{\mathbf{R}}-\underline{\mathbf{R}}\underline{\mathbf{R}}\underline{\mathbf{R}})$ ROBOT LEG

The inverse kinematic problem of the i th $\underline{\mathbf{R}}(\underline{\mathbf{R}}\underline{\mathbf{R}}-\underline{\mathbf{R}}\underline{\mathbf{R}}\underline{\mathbf{R}})$ robot leg is solved in two steps. First, the inverse kinematics of the serial part of the leg, which contains the first link (link $i1$) and the links along vectors \mathbf{s}_{i2} and \mathbf{s}_{i3} , is solved. This is straightforward and yields at most four different sets of solutions for θ_{i1} and θ_{i2} . Second, angle θ_{i3} is obtained. The vector loop equation of the five-bar linkage included in the leg is written as

$$\mathbf{s}_{i2} + \mathbf{s}_{i7} = \mathbf{s}_{i6} + \mathbf{s}_{i5} \quad (\text{B.1})$$

where \mathbf{s}_{i7} is given in (A.16). One then obtains

$$\mathbf{s}_{i5} = \mathbf{v}_i - \mathbf{s}_{i6} \quad (\text{B.2})$$

where $\mathbf{v}_i = \mathbf{s}_{i2} + \mathbf{s}_{i7}$. The squared length of \mathbf{s}_{i5} can be written as

$$\mathbf{s}_{i5}^T \mathbf{s}_{i5} = l_{i5}^2 = (\mathbf{v}_i - \mathbf{s}_{i6})^T (\mathbf{v}_i - \mathbf{s}_{i6}). \quad (\text{B.3})$$

That is to say

$$2\mathbf{v}_i^T \mathbf{s}_{i6} + (l_{i5}^2 - l_{i6}^2 - \mathbf{v}_i^T \mathbf{v}_i) = 0 \quad (\text{B.4})$$

where

$$l_{i6}^2 = \mathbf{s}_{i6}^T \mathbf{s}_{i6}. \quad (\text{B.5})$$

Vector \mathbf{s}_{i6} can be obtained as

$$\mathbf{s}_{i6} = \mathbf{Q}_i \mathbf{s}_{i6,l} \quad (\text{B.6})$$

where \mathbf{Q}_i is the rotation matrix corresponding to the orientation of the local frame located at the two revolute joints with coaxial axes—whose y -axis is in the opposite direction of the unit vectors \mathbf{e}_{i2} and \mathbf{e}_{i3} and whose z -axis is along the unit vector \mathbf{e}_{i1} —with respect to the base frame, $Oxyz$. It can be observed that matrix \mathbf{Q}_i is a function of just the variable θ_{i1} . Also

$$\mathbf{s}_{i6,l} = \begin{bmatrix} l_{i6} \cos \theta_{i3} \\ l_{i6} \sin \theta_{i3} \\ 0 \end{bmatrix} \quad (\text{B.7})$$

is the vector \mathbf{s}_{i6} expressed in the above-mentioned local frame. Substituting (B.6) and (B.7) into (B.4) leads to

$$2\mathbf{v}_i^T \mathbf{Q}_i \mathbf{e}_1 l_{i6} \cos \theta_{i3} + 2\mathbf{v}_i^T \mathbf{Q}_i \mathbf{e}_2 l_{i6} \sin \theta_{i3} + (l_{i5}^2 - l_{i6}^2 - \mathbf{v}_i^T \mathbf{v}_i) = 0 \quad (\text{B.8})$$

in which

$$\mathbf{e}_1 = \begin{bmatrix} 1 \\ 0 \\ 0 \end{bmatrix}, \quad \mathbf{e}_2 = \begin{bmatrix} 0 \\ 1 \\ 0 \end{bmatrix}. \quad (\text{B.9})$$

Equation (B.8) can be rewritten as

$$G_i \cos \theta_{i3} + H_i \sin \theta_{i3} + I_i = 0 \quad (\text{B.10})$$

with

$$G_i = 2\mathbf{v}_i^T \mathbf{Q}_i \mathbf{e}_1 l_{i6} \quad (\text{B.11})$$

$$H_i = 2\mathbf{v}_i^T \mathbf{Q}_i \mathbf{e}_2 l_{i6} \quad (\text{B.12})$$

$$I_i = l_{i5}^2 - l_{i6}^2 - \mathbf{v}_i^T \mathbf{v}_i. \quad (\text{B.13})$$

Applying the tangent half-angle formula to $\cos \theta_{i3}$ and $\sin \theta_{i3}$, one can then obtain

$$(I_i - G_i)T_i^2 + 2H_iT_i + (I_i + G_i) = 0 \quad (\text{B.14})$$

where

$$T_i = \tan \frac{\theta_{i3}}{2}. \quad (\text{B.15})$$

Two different solutions can be obtained for θ_{i3} from (B.14) and at last a maximum number of eight different inverse kinematic solutions can be obtained for the $\underline{R}(\underline{RR}\text{-}\underline{RRR})$ robot leg.

ACKNOWLEDGMENT

The authors would like to thank Simon Foucault for his help with the experiments and videos.

REFERENCES

- [1] A. Cherubini, R. Passama, A. Crosnier, A. Lasnier, and P. Fraise, "Collaborative manufacturing with physical human–robot interaction," *Robot. Comput.-Integr. Manuf.*, vol. 40, pp. 1–13, 2016.
- [2] D. V. Gealy *et al.*, "Quasi-direct drive for low-cost compliant robotic manipulation," in *Proc. IEEE Int. Conf. Robot. Autom.*, May 2019, pp. 437–443.
- [3] G. A. Pratt, M. M. Williamson, P. Dillworth, J. Pratt, and A. Wright, "Stiffness isn't everything," in *Experimental Robotics IV*. Berlin, Germany: Springer, 1997, pp. 253–262.
- [4] A. Albu-Schäffer *et al.*, "The DLR lightweight robot: Design and control concepts for robots in human environments," *Ind. Robot. An Int. J.*, vol. 34, no. 5, pp. 376–385, 2007.
- [5] S. D. Eppinger *et al.*, "Three dynamic problems in robot force control," *IEEE Trans. Robot. Autom.*, vol. 8, no. 6, pp. 751–758, Dec. 1992.
- [6] P. Fauteux, M. Lauria, B. Heintz, and F. Michaud, "Dual-differential rheological actuator for high-performance physical robotic interaction," *IEEE Trans. Robot.*, vol. 26, no. 4, pp. 607–618, Aug. 2010.
- [7] H. Sadjadian and H. D. Taghirad, "Impedance control of the hydraulic shoulder a 3-dof parallel manipulator," in *Proc. IEEE Int. Conf. Robot. Biomimetics.*, 2006, pp. 526–531.
- [8] F. Caccavale, B. Siciliano, and L. Villani, "The tricept robot: Dynamics and impedance control," *IEEE/ASME Trans. Mechatronics*, vol. 8, no. 2, pp. 263–268, Jun. 2003.
- [9] H. Z. Arabshahi and A. B. Novinzadeh, "Impedance control of the 3RPS parallel manipulator," in *Proc. 2nd RSI/ISM Int. Conf. Robot. Mechatron.*, 2014, pp. 486–492.
- [10] A. Dutta, D. H. Salunkhe, S. Kumar, A. D. Udai, and S. V. Shah, "Sensorless full body active compliance in a 6 dof parallel manipulator," *Robot. Comput.-Integr. Manuf.*, vol. 59, pp. 278–290, 2019.
- [11] C. Gosselin, T. Laliberté, and A. Veillette, "Singularity-free kinematically redundant planar parallel mechanisms with unlimited rotational capability," *IEEE Trans. Robot.*, vol. 31, no. 2, pp. 457–467, Apr. 2015.
- [12] L.-T. Schreiber and C. Gosselin, "Schönflies motion parallel robot (SPARA): A kinematically redundant parallel robot with unlimited rotation capabilities," *IEEE/ASME Trans. Mechatronics*, vol. 24, no. 5, pp. 2273–2281, Oct. 2019.
- [13] C. Gosselin and L.-T. Schreiber, "Kinematically redundant spatial parallel mechanisms for singularity avoidance and large orientational workspace," *IEEE Trans. Robot.*, vol. 32, no. 2, pp. 286–300, Apr. 2016.
- [14] L.-T. Schreiber and C. Gosselin, "Exploiting the kinematic redundancy of a (6+3) degree-of-freedom parallel mechanism," *ASME J. Mechanisms Robot.*, vol. 11, no. 2, 2019, Art. no. 021005.
- [15] B. Monsarrat and C. Gosselin, "Singularity analysis of a three-leg six-degree-of-freedom parallel platform mechanism based on Grassmann line geometry," *Int. J. Robot. Res.*, vol. 20, no. 4, pp. 312–328, Apr. 2001.
- [16] B. Monsarrat and C. M. Gosselin, "Workspace analysis and optimal design of a 3-leg 6-dof parallel platform mechanism," *IEEE Trans. Robot. Autom.*, vol. 19, no. 6, pp. 954–966, Dec. 2003.
- [17] K. Wen, D. Harton, T. Laliberté, and C. Gosselin, "Kinematically redundant (6+3)-dof hybrid parallel robot with large orientational workspace and remotely operated gripper," in *Proc. IEEE Int. Conf. Robot. Autom.*, 2019, pp. 1672–1678.
- [18] C. Gosselin and J. Angeles, "Singularity analysis of closed-loop kinematic chains," *IEEE Trans. Robot. Autom.*, vol. 6, no. 3, pp. 281–290, Jun. 1990.
- [19] D. Zlatanov, R. Fenton, and B. Benhabib, "A unifying framework for classification and interpretation of mechanism singularities," *ASME J. Mech. Des.*, vol. 117, no. 4, pp. 566–572, 1995.
- [20] D. Zlatanov, I. A. Bonev, and C. Gosselin, "Constraint singularities of parallel mechanisms," in *Proc. IEEE Int. Conf. Robot. Autom.*, vol. 1, 2002, pp. 496–502.
- [21] M. Conconi and M. Carricato, "A new assessment of singularities of parallel kinematic chains," *IEEE Trans. Robot.*, vol. 25, no. 4, pp. 757–770, Aug. 2009.
- [22] L.-T. Schreiber and C. Gosselin, "Passively driven redundant spherical joint with very large range of motion," *ASME J. Mechanisms Robot.*, vol. 9, no. 3, 2017, Art. no. 031014.
- [23] B. Siciliano, "Kinematic control of redundant robot manipulators: A tutorial," *J. Intell. Robot. Syst.*, vol. 3, no. 3, pp. 201–212, 1990.
- [24] C. M. Gosselin, J. Sefrioui, and M. J. Richard, "Solutions polynomiales au problème de la cinématique directe des manipulateurs parallèles plans à trois degrés de liberté," *Mechanism Mach. Theory*, vol. 27, no. 2, pp. 107–119, 1992.
- [25] K. Wen and C. M. Gosselin, "Forward kinematic analysis of kinematically redundant hybrid parallel robots," *J. Mechanisms Robot.*, vol. 12, no. 6, pp. 1–9, 2020.
- [26] I. A. Bonev, D. Zlatanov, and C. M. Gosselin, "Advantages of the modified Euler angles in the design and control of PKMs," in *Proc. Parallel Kinematic Mach. Int. Conf.*, 2002, pp. 199–215.
- [27] M. Isaksson, C. Gosselin, and K. Marlow, "An introduction to utilising the redundancy of a kinematically redundant parallel manipulator to operate a gripper," *Mechanism Mach. Theory*, vol. 101, pp. 50–59, 2016.
- [28] P. Fauteux, M. Lauria, B. Heintz, and F. Michaud, "Dual-differential rheological actuator for high-performance physical robotic interaction," *IEEE Trans. Robot.*, vol. 26, no. 4, pp. 607–618, Aug. 2010.
- [29] R. J. Anderson and M. W. Spong, "Hybrid impedance control of robotic manipulators," *IEEE J. Robot. Autom.*, vol. 4, no. 5, pp. 549–556, Oct. 1988.



Kefei Wen received the B.S. and M.S. degrees from the Yeungnam University, Gyeongsan, Republic of Korea, in 2012 and 2015, respectively, and the Ph.D. degree from Université Laval, Québec, Canada, in 2020, all in mechanical engineering.

His main research interests include robot kinematics and physical human–robot interaction.



Tan Sy Nguyen received the B.Eng. and M.Eng. degrees in automatic control from Ho Chi Minh University of Technology (HCMUT), Ho Chi Minh City, Vietnam, in 2013 and 2016, respectively. He is currently working toward the Ph.D. degree in mechanical engineering at the Robotics Laboratory, Université Laval, Québec, Canada.

He has been with the Department of Control Engineering and Automation, HCMUT since 2015. His interests include system modeling and control as well as human–robot interaction and its applications.



David Harton received the B.Eng. and master's degrees in mechanical engineering from Université Laval, Québec, Canada, in 2017 and 2020, respectively. He received the master's degree from the Robotics Laboratory, Université Laval, where he worked on the mechanical design of a kinematically redundant spatial hybrid parallel robot.

During his bachelor's studies, he completed internships in the Robotics Laboratory, Université Laval, where he developed sequentially actuated robots. His research interests include kinematic and dynamic modeling and design of mechanisms and robots.

Mr. Harton received postgraduate scholarships from the Natural Sciences and Engineering Research Council of Canada (NSERC) and the *Fonds québécois de la recherche sur la nature et les technologies* (FRQNT).



Thierry Laliberté received the B.Eng. and master's degrees in mechanical engineering from Université Laval, Québec, Canada, in 1992 and 1994, respectively.

Since 1994, he has been a Research Engineer with the Robotics Laboratory, Department of Mechanical Engineering, Université Laval. He is the author of a book and several published articles. His main research interests are self-adaptive grippers, prosthetic hands, static balancing, dynamic balancing, cable-driven mechanisms, and human-friendly robots.

Mr. Laliberté is a Registered Professional Engineer in the province of Québec. He was awarded a postgraduate scholarship by the Natural Sciences and Engineering Research Council of Canada (NSERC) for the master's degree.



Clément Gosselin (Fellow, IEEE) received the B.Eng. degree in mechanical engineering from the Université de Sherbrooke, Québec, Canada, in 1985, and the Ph.D. degree in mechanical engineering from McGill University, Montréal, Québec, Canada, in 1988.

He was a Postdoctoral Fellow with INRIA, Sophia-Antipolis, France, from 1988 to 1989. In 1989, he was appointed by the Department of Mechanical Engineering, Université Laval, Québec, Canada, where he has been a Full Professor since 1997. He was a Visiting Researcher with the RWTH, Aachen, Germany, in 1995, with the University of Victoria, Victoria, Canada in 1996, and with the IRCCyN, Nantes, France, in 1999. His research interests include kinematics, dynamics, and control of robotic mechanical systems with a particular emphasis on the mechanics of grasping, the kinematics and dynamics of parallel manipulators, and the development of human-friendly robots and haptic devices. His work in the aforementioned areas has been the subject of numerous publications in international journals and conferences as well as of several patents and two books. He has been directing many research initiatives, including collaborations with several Canadian and foreign high-technology companies, and he has trained more than 120 graduate students.

Dr. Gosselin was the recipient of several awards including the ASME DED Mechanisms and Robotics Committee Award in 2008, the ASME Machine Design Award in 2013, and the IFTOMM Award of Merit in 2019. He was appointed Officer of the Order of Canada in 2010 for contributions to research in parallel mechanisms and underactuated systems. He is a Fellow of the ASME and the Royal Society of Canada. He has been holding the Canada Research Chair in Robotics and Mechatronics since 2001. He is currently an Associate Editor for the *ASME Journal of Mechanisms and Robotics* and a Senior Editor for the *IEEE Robotics and Automation Letters*.

Dr. Gosselin was the recipient of several awards including the ASME DED Mechanisms and Robotics Committee Award in 2008, the ASME Machine Design Award in 2013, and the IFTOMM Award of Merit in 2019. He was appointed Officer of the Order of Canada in 2010 for contributions to research in parallel mechanisms and underactuated systems. He is a Fellow of the ASME and the Royal Society of Canada. He has been holding the Canada Research Chair in Robotics and Mechatronics since 2001. He is currently an Associate Editor for the *ASME Journal of Mechanisms and Robotics* and a Senior Editor for the *IEEE Robotics and Automation Letters*.